Scientific Reports

https://doi.org/10.1038/s41598-026-42212-9

Article in Press

A fully implantable intraspinal microstimulation device for early preclinical evaluation of feasibility, stability, and functionality

Received: 26 October 2025

Accepted: 24 February 2026

Published online: 24 March 2026

Cite this article as: Mirkiani S., O'Sullivan C.L., Arefadib A. *et al.* A fully implantable intraspinal microstimulation device for early preclinical evaluation of feasibility, stability, and functionality. *Sci Rep* (2026). https://doi.org/10.1038/s41598-026-42212-9

Soroush Mirkiani, Carly L. O'Sullivan, Amin Arefadib, Neil Tyreman, Katalin Sari, Don Wilson, Omar Tawakol, Philip R. Troyk, Richard Fox & Vivian K. Mushahwar

A Fully Implantable Intraspinal Microstimulation Device for Early Preclinical Evaluation of Feasibility, Stability, and Functionality

Soroush Mirkiani[1,2], Carly L O'Sullivan[1,2], Amin Arefadib[1,2], Neil Tyreman[2,3], Katalin Sari[2,3], Don Wilson[2,3], Omar Tawakol[2,4], Philip R Troyk[2,4], Richard Fox[2,5], and Vivian K Mushahwar[1,2,3*]

[1]Neuroscience and Mental Health Institute, University of Alberta, Edmonton, Canada
[2]Institute for Smart Augmentative and Restorative Technologies and Health Innovations (iSMART), University of Alberta, Edmonton, Canada
[3]Division of Physical Medicine and Rehabilitation, Department of Medicine, University of Alberta, Edmonton, Alberta, Canada
[4]Department of Biomedical Engineering, Illinois Institute of Technology, Chicago, USA
[5]Division of Neurosurgery, Department of Surgery, University of Alberta, Edmonton, AB, Canada

*Corresponding Author: Vivian.Mushahwar@ualberta.ca

Abstract

Electrical stimulation of the spinal cord has shown promise in restoring standing and walking after paralysis, yet key challenges remain in achieving selective and stable movements over long durations of stimulation. Intraspinal microstimulation (ISMS) provides precise and sustained activation of motor circuits in animal models. Nevertheless, translation of ISMS to humans requires assessment of surgical feasibility, safety and long-term stability in an animal model with spine and spinal cord size and morphology similar to those in humans. Here, we demonstrate the development and implementation of a fully implantable, wirelessly controlled ISMS device as well as its feasibility of implantation and functionality in domestic pigs. The ISMS implants contained strain relief mechanisms to improve mechanical compliance and minimize foreign body response. We tested the device in 4 pigs for periods of 8 to 14 days to assess surgical feasibility and early implant stability. Following implantation, stimulation through the electrodes successfully generated functional muscle contractions, graded movements around the hip, knee, and ankle joints. Post-mortem magnetic resonance imaging of the spinal cord revealed that the electrodes remained in place. All animals implanted with the device experienced transient motor paralysis post-implantation,

with recovery of muscle strength and coordination after one week. Immunohistochemical analysis revealed that glial encapsulation around the electrodes was confined to a 200 μm region from the center of the implantation sites and showed no migration of the implant. This suggests that the transient deficits are likely the effects of the surgical procedure (laminectomy, durotomy and spinal cord manipulation), although a contribution from the penetrating electrodes cannot be excluded. Such complications can be minimized by optimized surgical protocols and the application of anti-inflammatory corticosteroids and epidural hemostatic agents. This work establishes the feasibility of ISMS for restoring standing and walking after spinal cord injury and demonstrates its capability of selectively targeting motor networks throughout the lumbar enlargement in a large-animal model.

Introduction

Spinal cord injury (SCI) is a life-altering condition, with an estimated 250,000–500,000 new cases occurring worldwide each year, and a persistently high incidence rate of traumatic SCI at 20–45 cases per million [1,2]. Epidemiological data indicate that, among individuals with neurologically complete SCI, paraplegia occurs more frequently than tetraplegia[3]. Epidural spinal cord stimulation (eSCS) of the lumbosacral region has demonstrated promising results in restoring motor function after SCI in humans. Early clinical studies showed that tonic eSCS could evoke rhythmic, step-like movements of the legs in individuals with complete paralysis[4]. More recently, studies have shown that eSCS combined with intensive physical therapy can restore overground stepping with assistive devices in a subset of study participants with complete chronic paraplegia[5–7]. Subsequent investigations revealed that individuals with SCI receiving anatomically-targeted, phasic eSCS to the lumbosacral region, can also regain the ability to step overground almost immediately after implantation[8,9].

Despite these advances, eSCS still faces certain limitations. One prominent challenge is its relatively low spatial selectivity, which can recruit undesired fibers across multiple spinal cord segments and even contralateral rootlets at higher stimulation amplitudes[8,10]. This is especially evident in the sacral segments, where the dense clustering of dorsal and ventral rootlets necessitates the use of customized layouts of multipolar electrode designs and configurations for current steering and selective recruitment[8]. The relatively low selectivity of eSCS also requires time-consuming mapping procedures to identify optimal electrode layout and anode-cathode configurations[8,10]. Computer simulations have also been employed to determine the optimal positioning of eSCS electrodes; however, even slight, unavoidable shifts as small as 1 mm in the position of the electrode array relative to the spinal cord can reduce selectivity by up to 50 percent[8]. In addition, eSCS requires high stimulation amplitudes (in some cases up to 40 volts) to overcome the highly conductive cerebrospinal fluid (CSF) to effectively stimulate the spinal cord[11].

Intraspinal microstimulation (ISMS) is another approach that has been explored extensively in animal models[12–26], demonstrating the potential for restoring standing and functional weight-bearing walking after SCI. ISMS involves implantation of penetrating hair-like electrodes inside the spinal cord parenchyma, typically targeting the ventral horn where locomotor-related neural networks reside[12,27,28]. Implanted electrodes have a precise influence on interneuronal networks and nearby motoneurons resulting in higher selectivity of single joint and multi-joint synergistic movements while requiring 3-5 times lower stimulation current amplitudes than eSCS[16,28–30]. Both ISMS and eSCS primarily activate motoneurons trans-synaptically via

larger-diameter afferent pathways. Although eSCS can approximate physiological recruitment, human EMG studies[31] have shown mixed or partially reversed recruitment depending on stimulation parameters, likely due to broad afferent activation and current spread in the subdural CSF layer. ISMS can recruit motor units in a near-normal physiological order resulting in shallower force generation curves than eSCS providing enhanced fatigue resistance[13,15,29,32]. The close proximity of the penetrating electrode tip to intraspinal motor networks within the ventral gray matter, including motoneurons, premotor neurons, propriospinal fibers, and other fibers in passage, enables spatially localized and selective recruitment of these intraspinal circuits[12,13,32,33]. ISMS therefore promises finer control over motor output, which could translate into more precise functional movements. Preclinical investigations over the past two decades provided a strong proof-of-concept that ISMS can produce functional locomotor movements such as standing and walking in intact, chronically spinalized, and decerebrated animal models[14,15,27]. In cats, chronic ISMS elicits sustained, weight-bearing, functional hindlimb movements by selectively activating specific motor circuits for up to 6 months[34].

Despite its promise, ISMS is inherently more invasive than eSCS, which raises important considerations regarding safety, stability, and feasibility. Chronic implantation of penetrating electrodes in the central nervous system induce a foreign body response (FBR) and form a glial scar encapsulating implanted electrodes in the brain and spinal cord[35–41]. Implantation of 30 µm platinum-iridium (Pt-Ir) microwire electrodes into rat spinal cord with 4h stimulation per day for 30 consecutive days caused limited gliosis around both stimulating and non-stimulating electrodes with no pronounced loss of neurons surrounding the electrodes[35]. These findings indicate that chronic ISMS may be well-tolerated by spinal cord tissue. Nonetheless, ensuring long-term stability of ISMS devices in a dynamic spinal cord environment (especially in large animals) is a significant engineering challenge. Humans and other large mammals exhibit a greater range of spinal cord extension and compression to that of small animals which may result in unstable electrodes[42,43]. Therefore, testing the feasibility, safety and functionality of ISMS in a clinically relevant, large animal model is a crucial step towards the translation of ISMS to humans.

ISMS in the lumbar and cervical enlargements have been previously tested in large animals such as non-human primates (NHPs) and porcine models[20,21,45–47]. Wireless floating arrays (WFMAs) implanted in the lumbar enlargement of domestic pigs successfully evoked movements in the hindlimbs[20]. Safety of intraspinal motor network mapping in the lumbar enlargement has been demonstrated in Yucatan minipigs[48]. More recently, a single implant integrating two WFMA chips was developed for implantation in the domestic pig lumbar enlargement, enabling bilateral stimulation of the spinal cord[22]. Chronic implantation of the system showed

electrochemical and mechanical stability of the implanted electrodes over 22 and 70-day experiments. Pigs were able to regain walking while damage to the spinal cord and gliosis around the electrodes was observed [22]. Moreover, this device is highly localized and can only generate a subset of the movements needed for functional walking.

The primary goal of the current study was to assess the surgical feasibility and early stability of a fully implantable ISMS system capable of activating the locomotor-related networks spread throughout the 5-cm long lumbar enlargement in pigs. Specifically, we addressed two key questions: (i) Can an ISMS implant with a strain-relief mechanism remain stable in the spinal cord of a large animal? (ii) Is the surgical procedure for implantation of an ISMS system covering the entire lumbar enlargement feasible? To address these questions, we developed a fully implantable, wirelessly controlled ISMS system that (i) spans the entire rostrocaudal extent of the lumbar enlargement in a large-animal model, (ii) integrates strain-relief engineered to accommodate maximal length changes in the pig's lumbosacral spinal cord (while maintaining the applied forces on the implanted electrodes below the threshold for dislodgement[43] and (iii) uses laser-microfabricated microwire electrodes with controlled tip geometry and surface area. We demonstrate the functionality, early stability and biocompatibility over 8-14 days in domestic pigs. Our approach builds upon previous work in both small and large animals and represents a critical step towards the translation of ISMS for human applications.

Results and Discussion

Overview of the fully implantable ISMS device with strain relief mechanism

Locomotor-related motor networks are functionally organized along the rostrocaudal axis of the lumbosacral enlargement across various species[12,33,49,50]. Therefore, to achieve selective hindlimb movements, the ISMS implant must incorporate a sparsely spaced electrode array spanning the length of the enlargement. Specifications for the electrode array (Fig. 1) are provided in the Supplementary Material. The array provided access to spatially-distributed motor networks controlling hip, knee, and ankle movements, and was capable of coordinated eliciting multi-joint movement synergies (Fig. 2).

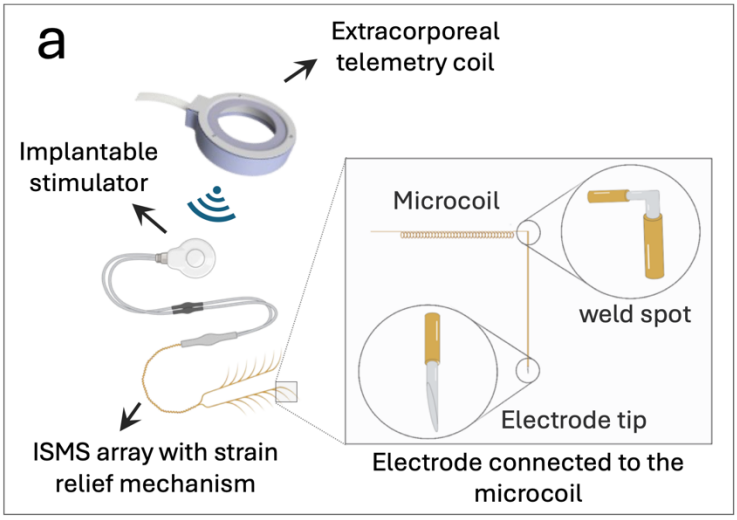

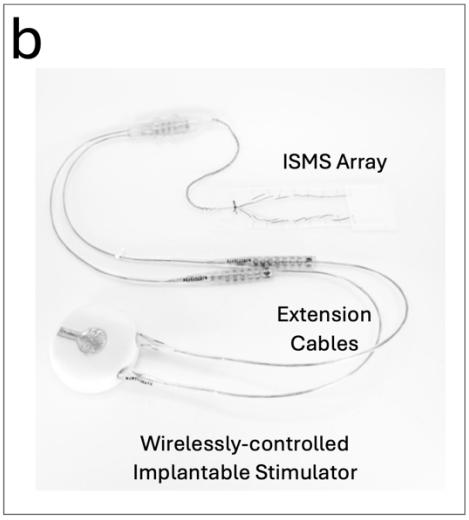

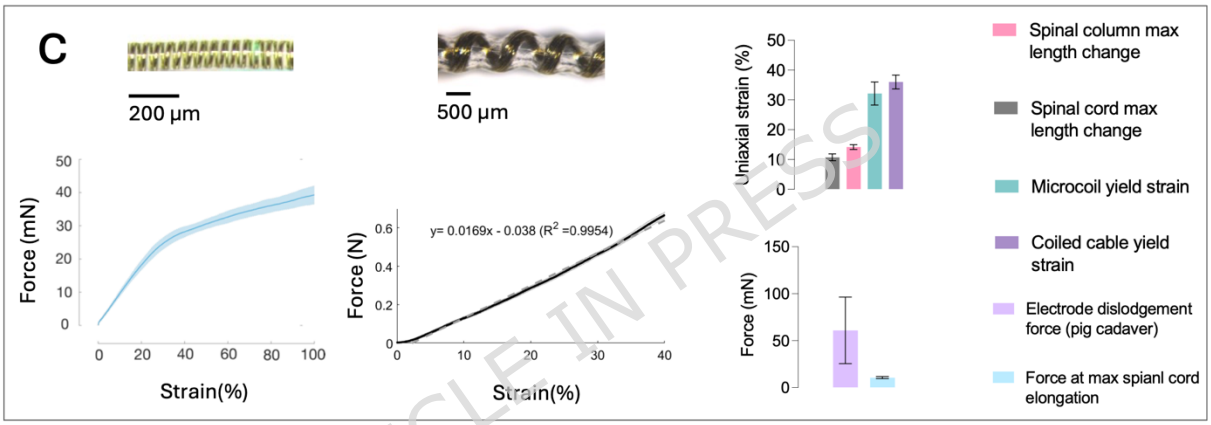

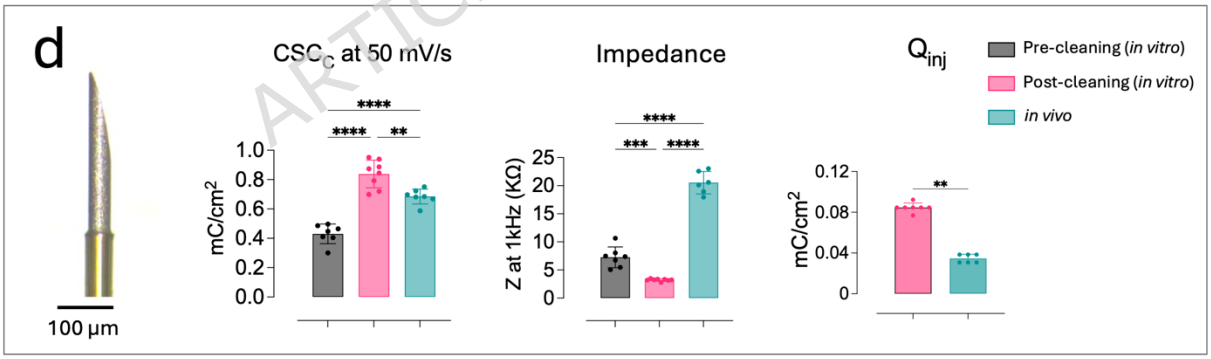

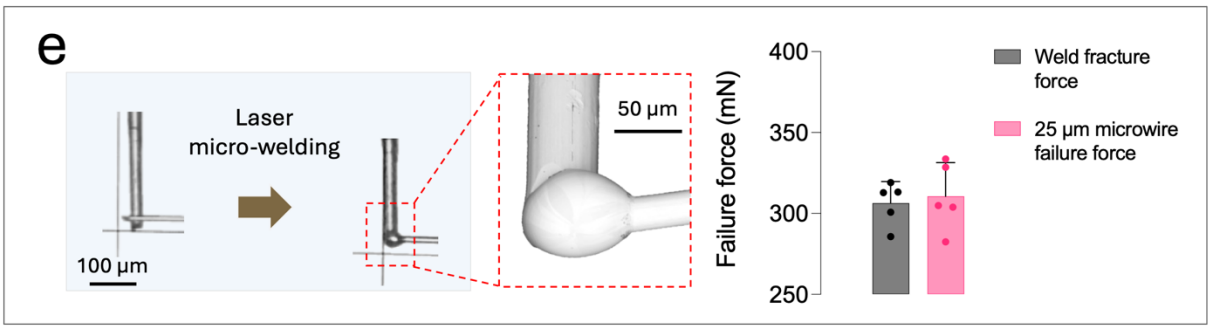

Fig. 1: Overview of the developed system. ***(a)*** *Schematics of the fully implantable ISMS device showing an extracorporeal coil transmitting power and data to the implantable stimulator connected to the ISMS array. The array contains a 14-channel coiled cable and microcoils in the leads attached to each electrode. Inset shows how microcoils are connected to the electrodes to provide strain relief.* ***(b)*** *Photo of the implantable system.* ***(c)*** *Optical images and mechanical properties of the microcoils and the coiled cable used to provide strain-relief. Bar graphs show the yield strain of the microcoils and coiled cables compared with maximum spinal cord and spinal column strains in the pig thoracolumbar region (top bar graph) as well as the comparison between electrode dislodgment force and the exerted force to electrodes at maximum spinal cord strain (bottom bar graph). The max spinal cord elongation value and electrode dislodgment forces were obtained from Toossi, et al[43].* ***(d)*** *Optical image of the electrode tip and electrochemical properties of electrodes prior to cleaning, after cleaning, and in vivo in pig spinal cord. Cathodic charge storage capacity (CSC_c) of electrodes, impedance magnitude at 1kHz and charge injection limit (Q_{inj}) are shown.* ***(e)*** *Optical images showing the laser welding process of the leads with microcoils (25µm microwires) to the electrodes (50µm microwire). Bar graph shows that joint breakage forces of welded samples are statistically similar to the failure force of the smaller (25 µm) microwire.*

Optimized electrode fabrication

We selected microwire technology for our proof-of-concept ISMS device due to its extensive use in both stimulation and recording in the central nervous system[14,15,35,46,51–53]. Historically, electrodes for ISMS were made from polyimide-insulated 30-50 µm Pt-Ir microwires, and have been de-insulated using mechanical methods, such as rubbing the insulation off between two glass slides or using a fine micrometer, introducing significant variability in the geometric surface area (GSA) of the exposed tip[54]. Manually beveling the tip with a scalpel or pipette beveler can also yield inconsistent angles and structural flaws at the tip of the microwire[54]. Defects at the insulation–metal interface can promote fluid ingress between the insulation and the metal shaft, altering both the GSA and the electrode's electrochemical properties[55]. Moreover, previous investigations revealed insulation fragments embedded in sectioned tissue, affecting the safety and longevity of these microwires for ISMS.[35,54].

To address these issues, we employed laser microfabrication for both insulation removal and tip beveling, improving electrode quality and GSA consistency. We compared nanosecond (ns) and femtosecond (fs) laser pulses for de-insulation, as well as laser cutting vs. mechanical polishing for beveling of the microwire tip (Extended Fig. 1). By optimizing laser power and scanning speed, the insulation was selectively removed without significantly ablating the underlying metal. We produced laser-induced periodic surface structures on the tip of the electrode using the fs laser, known to enhance neural probe electrochemical properties[56]. Atomic force microscopy and optical profilometry confirmed that the fs-deinsulated electrodes exhibited greater surface roughness leading to higher electrochemical surface area (Extended Fig. 2). Among beveling methods, mechanical polishing yielded the smoothest surface, followed by fs laser and ns laser cutting. Ultimately, we selected the fs laser for both deinsulation and beveling at ~15°, maintaining a consistent GSA of 65,002 ± 4,431 µm² (mean ± SD, n = 20), sufficient for safe charge injection at current amplitudes eliciting functional limb movements.

After fabrication, the electrodes underwent electrochemical cleaning to remove adsorbed organic contaminants from the ablated insulation, enhancing the slow seep rate (50 mV/s) cathodic charge storage capacity (CSCc) and reducing the impedance by factors of 1.57 and 2.24. (Fig. 1d, Extended Fig. 2). The CSCc was 0.43 mC/cm^2 pre-cleaning (in vitro), 0.83 mC/cm^2 post-cleaning (in vitro) and 0.68 mC/cm^2 in vivo. Impedance measurements were 7.3 ± 1.8 kΩ pre-cleaning (in vitro), 3.2 ± 2.1 kΩ post-cleaning (in vitro), and 20.5 ± 2.0 kΩ in vivo at 1kHz. The charge injection capacity (Q_{inj}) was 85 µC/cm² in vitro (post-cleaning) and 35 µC/cm² in vivo, sufficient to deliver stimulation currents of 125 µA and reliably elicit functional limb movements while remaining within the water window (Extended Fig. 2).

Strain-relief mechanism using microcoils

Mechanical stability is critical for implantable devices such as cardiac pacemaker electrodes, eSCS, deep brain stimulators (DBS), and nerve or muscle stimulating/recording devices[57–62]. A simple strain-relief loop in the extension cable is recommended to prevent mechanical failure by accommodating motion and reducing stress at connection points[61,63,64]. The addition of helically coiled cables can reduce the amount of load on the anchor point by a factor of three[61]. Coiled cables have been used in neural interfaces due to their omnidirectional flexibility, reducing stress during torsion, twisting and bending; robust electrical performance; and superior fatigue resistance[41,65].

We added strain relief in the leads connected to individual implanted electrodes by integrating microcoils (OD: 190 µm, length: 7 mm) fabricated from 25 µm insulated Pt-Ir microwires. The microcoils were additionally encapsulated in PDMS to prevent tissue ingrowth that can compromise their stretchability. The design criteria for the microcoils were to: (i) remain elastic under up to ~11[43] % spinal cord elongation from hyperextended to hyperflexed positions (with a safety factor ≥ 2); (ii) transmit forces well below the electrode-dislodgement threshold (~60.9 ± 35.5 mN, critical dislodgement ≈ 25.4 mN); and (iii) maintain uniform PDMS coating. Zero-pitch coils lacked sufficient elasticity, and coils dip-coated at 20 mm/min (P20) exhibited poor PDMS coverage. In contrast, microcoils with a 30–40 µm pitch, dip-coated at 5 mm/min (P5), achieved an exerted force of 10.5±1.1 mN at 11 % elongation that is less than half of the critical dislodgement force. This microcoil design ensures that physiological spinal movements do not approach levels that could dislodge the electrodes or damage surrounding tissue.

We further incorporated a coiled cable comprising 14 individually insulated microwires (25µm, Pt-Ir) to accommodate the macromotion between the tethered points on L3 spinous process and the exit point at the dura

mater[43]. The bundle was coiled in a pre-stretched silicone tube, which was then relaxed and filled with polydimethylsiloxane (PDMS). This provided a multilayer dielectric insulation and additional mechanical strain-relief for the microwires. The coiled cable had <0.8 mm outer diameter, which is substantially smaller than commercially available lead systems for eSCS, DBS and cochlear implants. This coiled cable was 10 cm long, allowing the neurosurgeon to include an additional strain relief loop as it exited the dura mater and was secured to the L3 spinous process. The cable was further protected by a 3D-printed biocompatible elastic grommet. Within the grommet, the coiled cable was connected to two Medtronic extension cables (Fig. 1b). Using electrochemical impedance spectroscopy (EIS), the capacitance of each microwire lead (with respect to the 13 other leads shorted) in the coiled cable measured at 1 kHz was 29 ± 0.2 pF (mean ± SD, n = 6). Stretching the coiled cable by up to 40% while immersed in phosphate-buffered saline (PBS) required an elongation force of 701 ± 12.8 mN and the capacitance between one microwire and remaining microwires in the coiled cable (~18 pF at 1kHz) did not change; Extended Fig. 2d).

Welding electrodes to the microcoilsAt the proximal end, each microcoil had a ~1 mm portion of straight 25µm microwire that was laser-welded to the electrode (50 µm) at an approximately 90° angle (Fig. 1e), such that when the electrodes were inserted into the spinal cord, the microcoils and associated leads lay flat on the pial surface. Electrodes were implanted in the neutral spinal position and additional slack in the leads with the microcoils further enhanced the design safety.

For laser welding, we selected the optimal weld parameters based on the maximum joint breakage force (JBF)[66]. We tested pulse widths of 0.5, 1, and 2 ms at various pulse powers of 75, 100, 150, 250, and 300 W. At 75 and 100 W, failure occurred at the 25 µm microwire indicating that the weld was stronger than the microwire, whereas higher powers resulted in failure at the weld junction indicating suboptimal joints (Extended Fig. 3b, 3c). The JBF at 100 W was statistically comparable to the breakage force of an isolated 25 µm microwire (Fig. 1e). Scanning electrode microscopy (SEM) and focused-ion-beam-SEM analyses confirmed a minimal heat affected zone and that the weld cross-sections were free of pores, microcracks, or impurities[67] (Extended Figure 3d).

Functional movements elicited by the fully implantable system

We tested implantation feasibility and acute functionality of the fully implantable device in 10 domestic pigs (51.8±5.4 kg). In acute experiments, we tested movement strength at charge densities exceeding the electrode's Q_{inj} threshold (≤125 µA), while for chronic experiments, we limited stimulation amplitudes to this maximum safe current. Movement kinematics

were recorded at three stimulation amplitudes of 100 μA, 200μA, and 300μA in deeply anesthetized pigs (Fig. 2a). Increase in stimulation amplitude significantly increased the absolute joint range of motion (ROM) for both ankle extension (AE; from 4.1±0.3 to 5.0±0.6˚ to 9.2±0.2; mean±SD) and flexion (AF; form 1.1±0.9˚ to 8.0±2.0˚ to 9.8±2.0˚). For knee extension (KE), the mean±SE of joint ROM significantly increased form 9.1±2.7˚ to 19.9±3.9˚ when increasing stimulation amplitude from 100 μA to 300 μA, resulting in full knee extension. In some locations the movement type changed with increase in stimulation amplitude (e.g., from AE to HE or AF to KE). These locations were deemed to be at the overlap of muscle motor pools, and by fine adjustment of electrode location, sustained movements were achieved over a range of stimulation amplitudes. The total ROM for each joint was obtained by summing the maximum flexion and extension values achieved (Fig. 2a). These total ROM values were comparable to the joint ROMs observed in Yucatan minipigs walking overground at slow speeds[68]. Previous studies of ISMS in domestic pigs have analyzed only a limited number of evoked movements[16,20,22,46]. Using ultrasound-guided implantation combined with the array's adaptive placement in the rostrocaudal, dorsoventral, and mediolateral axes along the entire lumbosacral region, we achieved precise generation of flexion and extension movements across the hip, knee, and ankle joints (Fig. 2).

The ability of the developed ISMS system to produce selective joint-specific activation is consistent with previous animal studies[14,15,21,49], and allows for the generation of all subphases of the walking cycle[15]. Moreover, we observed multi-joint and single joint movements similar to previous ISMS studies that demonstrated stimulation through a single electrode within the cervical or lumbar enlargement can evoke synergistic multi-joint movements (for example, forelimb reach-and-grasp movements[28] or forward, upward, downward and backward hindlimbs synergistic [15,27,69]) as well as isolated single joint movements[12,15,28,32,45,49,70].

Analysis of isometric joint forces of the evoked movements demonstrated a graded relationship between stimulation amplitudes and resultant isometric forces, indicating a predictable and controllable response across the range tested. ISMS generated strong movements at maximal amplitude with peak forces of 27.4±6.8 N, 11.0±2.3 N, 15.4±1.2 N, 17.6±0.5 N, 4.7±0.3 N, and 2.8±0.3 N for HE, HF, KE, KF, AE, and AF, respectively (Fig. 2b). For all of the evoked movements, increase in stimulation amplitude consistently and gradually increased the isometric joint forces consistent with previously observed results in feline and pig models[13,21].

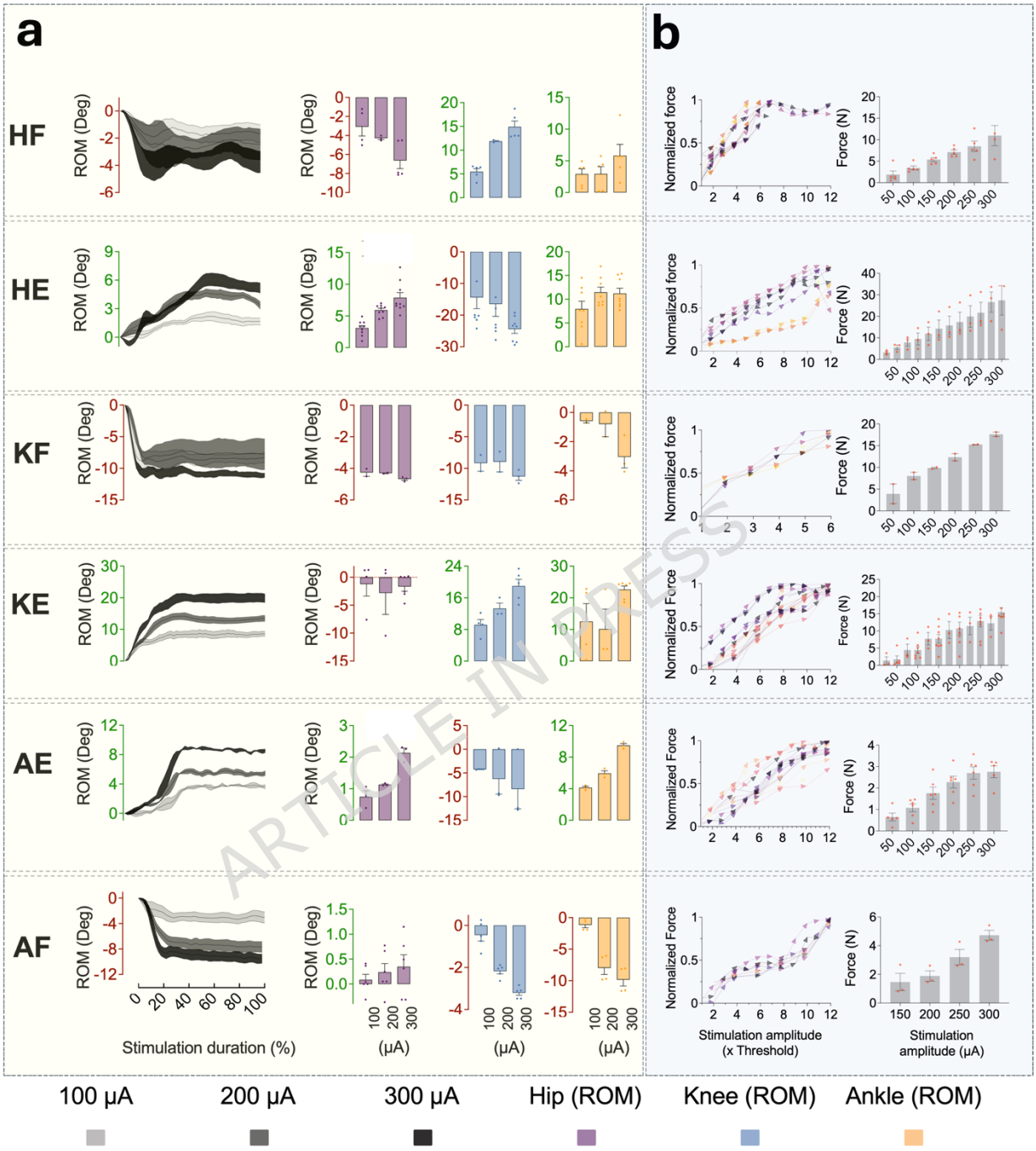

Fig. 2: Joint kinematics and isometric forces of the evoked movements. (a) *Joint angles of the hip, knee, and ankle are shown during hip flexion (HF), hip extension (HE), knee flexion (KF), knee extension (KE), ankle flexion (AF), and ankle extension (AE) movements elicited by ISMS through single electrodes with amplitudes of 100, 200, and 300 μA. Joint angles associated with each movement are sorted in rows. The left graph for each movement shows how the range of motion (ROM) of the joint being flexed/extended changed during the stimulation duration of 1 second. Shaded area shows the standard error of mean. The ROM values of hip, knee, and ankle are shown for each movement at various stimulation amplitudes of 100, 200, and 300 μA. Individual dots show*

*averaged values (from three trials) from one animal. The legs were freely hanging during movements except for KE and HF movements where the knee and hip joints were pre-flexed and pre-extended, respectively, using a pulley system[49]. **(b)** Isometric joint forces at stimulation amplitudes ranging from 25 to 300 µA for each of the evoked movements. The left graph shows the normalized force values versus multiples of threshold from individual movements. Each color shows data collected from one electrode at various stimulation amplitudes. Arrow heads show the slope of the recruitment curve at each multiplication of threshold amplitude. The right graph shows the isometric force values with respect to stimulation amplitudes for each movement. Error bars show standard error of the mean and individual dots show average force values (three trials) collected in one animal.*

The Sigmoidal fit to the average data across all animals for each movement showed a shallow force recruitment curve hillslope (<1.6). Precise modulation of intraspinal networks with ISMS has proven to produce consistent and reproducible muscle forces through transsynaptic activation of motor networks by activating afferent, propriospinal and intraneuronal fibers in passage traveling in the ventral horn[12,13,15,32,45,71]. Penetrating electrodes recruit axons at lower current than neuronal cell bodies[72,73]. Gaunt et al[32] showed that ISMS in cat lumbar spinal cord can activate motoneurons directly only at high current amplitudes. Also, ISMS can trigger antidromic conduction towards the dorsal root ganglions (DRGs) followed by orthodromic propagation across several segments through the muscle-specific Ia-reflex pathways generating trans-synaptic natural muscle synergies[32]. Experimental and computational studies show that eSCS also recruits motoneurons transsynaptically[9,74,75]. However, lower gradation range has been reported for eSCS compared with ISMS in the cervical region in NHP models[29]. In addition, EMG recording and nerve conduction velocity measurements in individuals with SCI have shown that tonic eSCS can recruit motoneurons both in a physiological (based on Henneman's size principle) and a reversed order[31]. Muscle fatigue can reduce contraction force over time, presenting challenges especially in the presence of external perturbations[76]. The precise control and fatigue-resistant movements enabled by ISMS hold significant clinical promise for achieving consistent, smooth movements after severe SCI.

Assessing the Safety and Stability of Short-Term Chronic Implantation

We evaluated the feasibility and early-stability of a fully implantable ISMS system in four domestic pigs (46.2±2.6 Kg), P1, P2, P3, and P4 with implantation durations of: 8, 8, 14, and 28 days, respectively. The chronic implantation periods were selected to focus on the early postoperative interval, during which spinal motion and acute inflammatory responses are expected to pose the highest risk for electrode displacement and tissue damage. Animal P4 was excluded from the stability and IHC analyses because post-surgical complications led to early array displacement (see post-operative animal care subsection in the Methods section); thus, P3 (14

days) provided the longest dataset for quantitative tissue analysis. These findings therefore represent early stability and early tissue responses rather than device lifetime performance, which needs be addressed in a dedicated chronic study over longer time scales.

The components of the developed array are shown in Fig. 3a. In the initial designs, a 200 µm-thick PDMS tab was used to anchor the device to the dentate ligaments (Fig. 3a). However, post-operative tissue histology revealed substantial compression of the L3 spinal cord segment in P1 where the PDMS tab was located (Fig. 3a right). Despite the small diameter of the microcoils (Fig. 3a-iii) occupying minimal space in the subdural area, we noticed adhesion of the microcoils to the dura mater after 8 days of implantation in P2 (Fig. 3b). Therefore, we removed the PDMS tab and incorporated a dural expansion procedure to increase the subdural space and prevent tissue attachment (Fig 3b – added artificial dura). Expansile duraplasty has been investigated as a way to relieve spinal cord compression, restore subarachnoid space, and improve neurological outcomes in patients with acute spinal cord injury[77,78] and may reduce spinal cord pressure in porcine models[79]. In addition, Duraplasty has been used in other recent works to enhance motor recovery after implantation surgery in pigs lumbar spinal cord[22].

Except for P1, pigs were able to stand and walk immediately after recovery from surgery one day post-surgery. However, the hindlimb motor control and reflexes were lost two days later. The withdrawal, panniculus, and perineal reflexes started to return 4-5 days post-surgery. All pigs retained normal bowel and bladder function indicating intact sacral autonomic circuitries. Caregivers assisted the animals to stand, starting from day 3 post-surgery to advance motor recovery. Animal P1 developed prolapse possibly due to constipation as a side effect of oral tramadol administration, which resulted in premature termination.

P1 and P2 exhibited acute paralysis equivalent to porcine thoracic injury score (PTIBS)[44] scores of 1–2 at the end of experiment duration (8 days). These animals were able to perform joint movements without any stepping or weight support. Animal P3, however, showed remarkable recovery 14 days post-surgery with frequent weight-supported walking (5-6 consecutive steps in the cage with minimal balance support) with occasional dorsal hoof placement (Fig 3c).

Overall, animals experienced transient neurological deficit with signs of recovery of motor control starting at 8-10 days post-surgery in P3 and P4.

ISMS array implantation in cats, trans-durally[34], or intra-durally[41] have not shown any neurological impairments after implanation. However, Yucatan minipigs that had undergone an intraspinal mapping with penetrating

electrodes, and the sham control animals receiving only the durotomy and laminectomy experienced similar transient deficits[48]. In addition, domestic pigs implanted with localized WFMA devices, and sham control domestic pigs receiving only durotomy and laminectomy showed temporary neurological impairments[22]. In another study, while performing cervical hemi-section (at C6 spinal cord level) in domestic pigs caused a permanent paralysis of the ipsilateral forelimb, the other 3 limbs also showed temporary paresis which fully recovered by the third week post-surgery[80]. The transient deficits seen in the current study were likely caused by spinal cord edema [81] or epidural hematoma[82, 83]. Administering corticosteroids to reduce inflammation, employing wound drains, administration of antifibrinolytic agent (such as Tranexamic acid), avoiding antiplatelet medications (such as nonsteroidal anti-inflammatory drugs) in the immediate peri-operative period, and use of epidural hemostatic agents can likely mitigate these effects. Although post-mortem MRI did not show evidence of electrode migration, tract hemorrhage or cavitation, the absence of a sham-operated control group or in vivo imaging in the current study precludes definitive separation of the contributions of surgical manipulation, postoperative edema or hematoma, and the presence of the implanted electrodes in the current study.

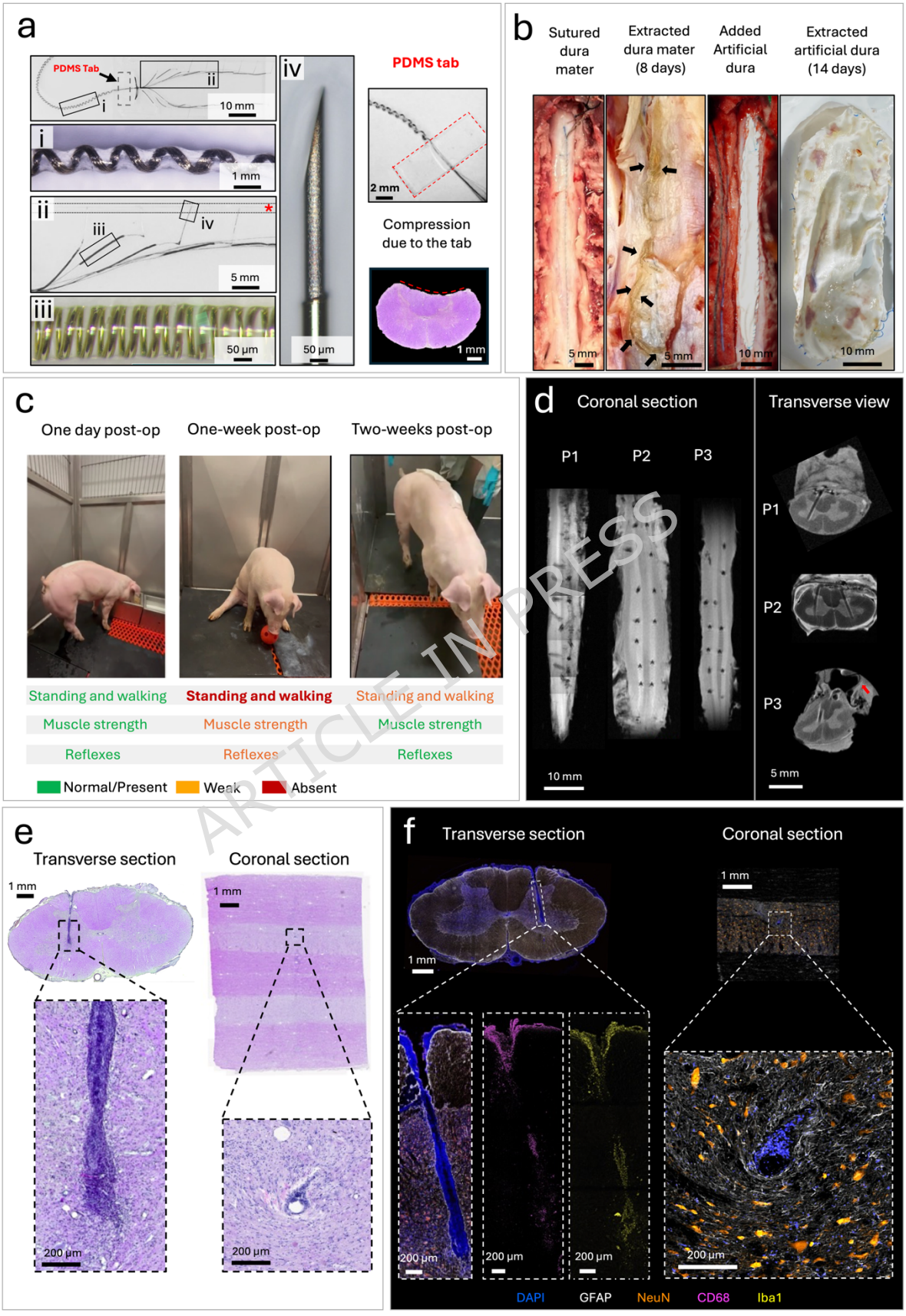

Fig. 3: Chronic response to the ISMS array implantation. (a) *Photo of the ISMS array with its components: The transparent PDMS tab outline is shown with dashed line in top left, i) coiled cable, ii) closer view of the microcoils connected to electrodes. Red asterisk shows the Silastic tube used for holding the electrodes during implantation, iii) microcoil, and iv) electrode tip. A closer view of the PDMS tab (dashed red line) and H&E image of tissue compression in response to the anchored tab to the dentate ligaments is shown in the right panel. The dashed lines in the H&E image show where the PDMS tab was located during implantation.* ***(b)*** *from left to right: closed dura mater after implantation, observing attachment of microcoils to the dura mater after 8 days of implantation (black arrows), incorporation of expansive duraplasty, and extracted artificial dura mater after 14 days showing no adherence of microcoils.* ***(c)*** *Transient neurological deficits and recovery observed after 14 days of device implantation. Lower leg paralysis and areflexia following the implantation surgery began recovering week 1 post-surgery with increased muscle strength and reflex recovery by week 2.* ***(d)*** *Coronal (left) and transverse (right) view of MRI images of excised spinal cord samples after 8- and 14-days following device implantation. All implanted electrodes remained in the tissue without dislodgment. P2 and P3 spinal cord samples were scanned with a longer coil resulting in smoother image, while P1 sample was manually moved in the coil to scan smaller segments resulting in poorer quality (see MRI section in methods). Outline of the artificial dura mater is show by red arrows in transverse view of P3 spinal cord* ***(e)*** *Low and high magnification images of H&E staining of spinal cord samples in transverse and coronal sections show the extent of scar formation around the electrodes.* ***(f)*** *Immunostaining of tissue showing neuronal loss, accumulation of activated macrophages and immune cells around the implanted electrodes surrounded by astrocytes in both transverse and coronal sections*

Immunohistochemical Analysis of Electrode-Tissue Interface

It is widely accepted that chronic implantation of non-degrading electrodes into the brain and spinal cord triggers a FBR characterized by acute trauma from insertion, disruption of the blood–spinal cord barrier, infiltration of immune cells, activation of glial cells, and eventual glial scar formation[35,84,85]. To date, glial scar formation around chronic penetrating electrodes in the pig spinal cord remains uncharacterized.

Fluorescent immunohistochemistry (IHC) revealed glial scarring around the implanted electrodes, generally confined within approximately 200 µm from the center of the electrode tract (Fig. 4, Extended Fig. 5). To quantify cellular composition of the area around implanted electrodes we performed IHC on coronal and transverse sections of explanted spinal cords using antibodies against CD68 (activated microglia /macrophages), Iba1 (microglia), GFAP (astrocytes), NF200 (axons), MBP (myelin), and NeuN (neuronal nuclei). Baseline fluorescence intensity was obtained at locations 750 µm way from the electrode tracks, enabling relative quantification of changes in fluorescence intensity near the tracks. We analyzed the maximum relative fluorescence intensity for each marker and the radial distance from the implant where the maximum occurs.

Across all sections (Fig. 4b, Extended Fig. 5), marker signals were essentially undetectable within a 25–30 µm radius void centered on the electrode track. NeuN and MBP signal intensities were further decreased in a ring 40-60 µm around this void while CD68, Iba1, and GFAP relative intensities showed a narrow peak within this ring (Extended Fig. 5). These

results suggest local neuronal and myelin disruption by the implanted 50 µm electrode, and the accumulation and activation of glial cells around it.

DAPI nuclear signal increased 3.1-fold at 68 ± 16 µm from the center of the electrode track, consistent with elevated cellular density adjacent to the implant. CD68, Iba1, NF200, and GFAP reached relative maxima at 61 ± 14 µm, 74 ± 19 µm, 82 ± 27 µm, and 105 ± 24 µm, corresponding to 3.0-, 1.7-, 2.0-, and 1.7-fold increases over the far-field baseline at 750 µm. These profiles indicate peri-electrode inflammatory cell accumulation and glial encapsulation.

NeuN and MBP signal intensities exhibited modest overshoots of approximately 1.2-fold at 293 ± 87 µm and 213 ± 87 µm, respectively. Because intensities are normalized to the far-field reference, these small peaks are best explained by redistribution and compaction of surviving parenchyma or myelin compaction during recovery, rather than new neurons or a net increase in myelin content.

Explanted electrodes showed adherent biological material under SEM. Hoechst staining revealed that the explanted electrodes contained cells (Extended Fig. 4), which were further identified to be activated macrophages and microglia using Cd68 and Iba1 staining, respectively. Similarly, explanted silicon intracortical electrodes in rats cortex were shown to have adhered cells including fragments of activated astrocytes[86–88] and compact microglial[39,87,88] cell layers after implantation periods as short as 1 day to 12 weeks. The electrode tip typically showed higher cell attachments than the insulation in this study which could be due to the high surface roughness of the tip created by fs laser patterning promoting cell adhesion (Extended Fig. 4d). Proper tissue adhesion can mitigate potential interfacial strain at the tip of the electrode[89].

Bamford et al[35] evaluated the spinal cord FBR after 30 days of microwire implantation (30 µm) in rats. They found elevated immunoreactivity to ED-1 (macrophages) in serial sections up to 200 µm rostrocaudal to the implanted microwires but not at 400 µm away sections. They found no difference in between the sham implanted microwires and the stimulating ones (up to 48 nC/phase, 4h/day for 30 days). We previously demonstrated that insertion wounds created by electrode penetrations in Yucatan minipig spinal cord cause minimal lasting glial scar and become histologically inconspicuous by four weeks post-injury[48]. Tawakol et al.[22] employed H&E staining to examine the chronic tissue response to localized WFMA implant in domestic pigs, revealing pronounced damage within the implantation zone, likely driven by the high electrode density in a confined area and the ceramic base connecting the electrodes. The sequence of cells observed around electrodes in the current study is consistent with previous works

investigating glial cell encapsulation and FBR to intraspinal[35,36,41], intracortical[36,38,39,87,90,91], and DBS implants[92,93]. Immediately adjacent to the electrode we found accumulation of activated microglia and macrophages, surrounded by activated astrocytes and localized neuronal, axonal, and myelin disruption. The FBR to the ISMS devices with strain relief in this study is comparable to that reported by Bamford et al.,[35] despite several differences between the two studies. We used larger microwires (50 μm diameter, 3.5–5 mm length versus 30 μm diameter, 1.2 mm length in Bamford et al. study) so that they can penetrate through the relatively thick pia mater in pigs without bucking. Contrary to our observation, Bamford et al.[35], reported insulation fragments in histological sections likely due to the manual de-insulation technique previously used[35]. Although Bamford et al. did not perform marker fluorescence intensity analysis, the comparable extent of tissue encapsulation in our pig model, despite its much larger spinal cord and greater macromotion (large scale movements) and micromotion (from respiration, pulsation, CSF pressure fluctuations)[43,65], points to a markedly improved tissue response.

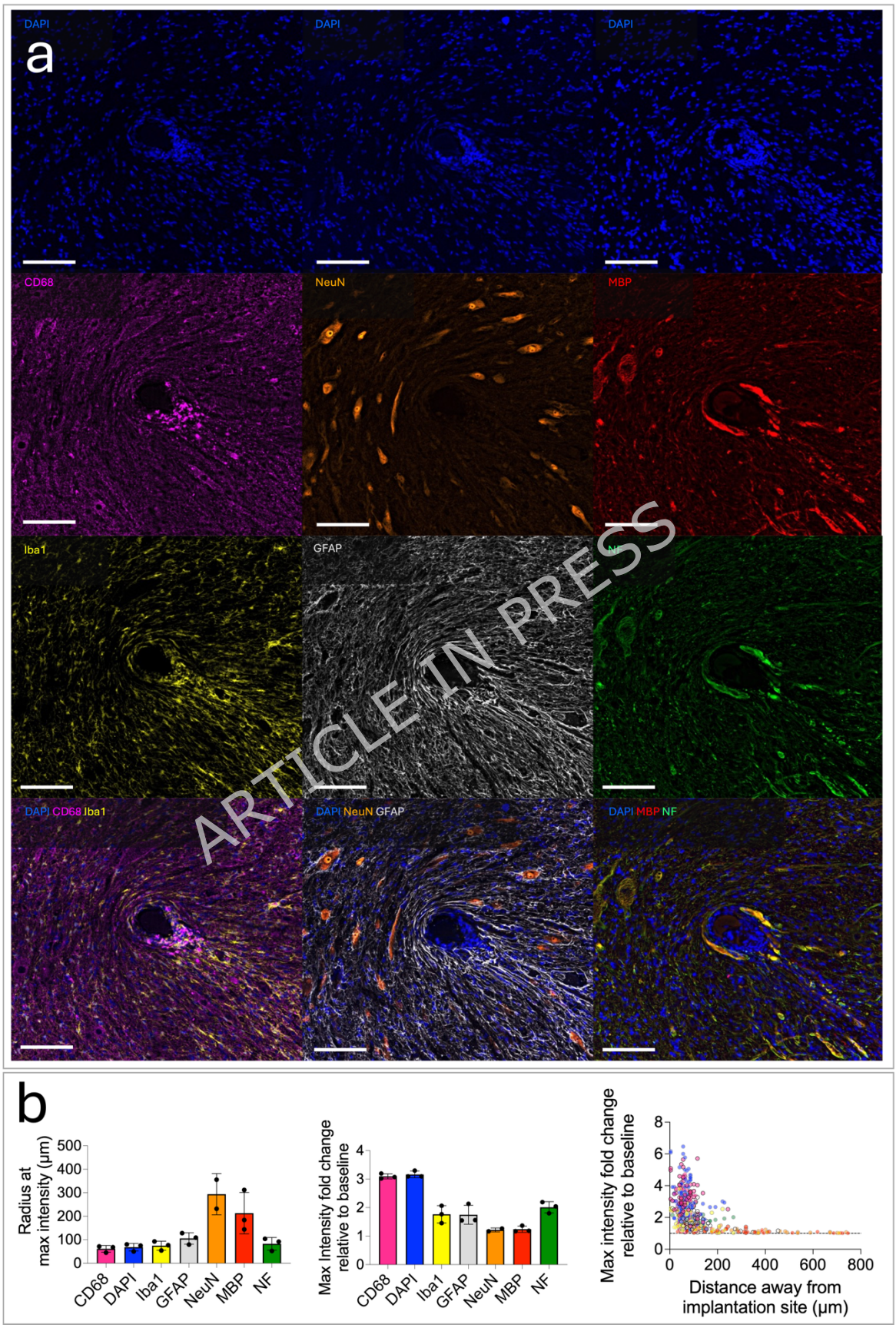

Fig 4. Immunohistochemical zonal analysis of tissue response to the electrode implantation: ***(a)*** *Representative immunohistochemical images of coronal sections containing electrode track. Nuclear staining with DAPI and tissue immunoreactivity to CD68, NeuN, MBP, NF, Iba1, GFAP, and NF are shown. The bottom row shows the overlay of all channels in each column. Different staining combinations were performed on neighboring sections 20µm and 40µm away. Scale bars are 100µm.* ***(b)*** *Radius at which maximum normalized intensity for each marker was calculated is shown in the left. The maximum normalized intensity for each marker is shown in the middle. NeuN and MBP markers show maximum intensity at around 200-300 µm away from the implantation site (left). However, NeuN and MBP maximum intensities are around 1 (middle) suggesting neuronal death and demyelination rather than accumulation of neurons or myelin base protein. This is shown in the right panel figure where it shows the relationship between maximum intensity relative to baseline versus the radial distance at which the maximum occurs for each marker.*

Nevertheless, encapsulation of chronically implanted electrodes forms an insulating sheath of hypertrophied reactive glial cells and fibroblasts that can electrically insulate the electrode from neurons[94], reduce local neuronal density, impede diffusion[95], and ultimately limit recording efficacy and require elevation in stimulation thresholds[40,87,88,96]. Despite this, stable cortical recordings over years after implantation have been reported[51,97]. In addition, functional measurement of force recruitment after chronic ISMS in rats remained comparable to intact controls despite the observed scar formation[35]. For current amplitudes of 100–200 µA used in ISMS, the strength–distance law[98,99] predicts an activation radius of 600-800 µm, well beyond the ~200–300 µm thickness of the astrocytic scar.

Chronic gliosis at the electrode–tissue interface is governed by various factors such as the probe size, stiffness, and the mechanical stresses transmitted through tethering and micromotion. Electrodes tethered to the skull induce more immunoreactivity compared with untethered, floating electrodes in rat cortex[87,100].Vomero et al.[101] demonstrated that flexible, smaller probes (50 µm× 12µm) or untethered electrodes elicit significantly less astrocytic and microglial activation than the flexible, larger (100µm × 12µm) or fixed ones. Luan et al,[102] demonstrated that ultra-miniaturized (10 µm × 1.5 µm) flexible probes achieve negligible scarring even when tethered. Both macro- and micro-motions contribute to the tissue damage by imposing interfacial stress between the implanted probes in the soft nervous tissue[65]. The mechanical stress can cause shear and compression of the surrounding tissue and initiate proinflammatory signaling[103,104]. The higher motions in the spinal cord compared with the brain can exacerbate the tissue response[28,92,93]. In this study, we incorporated strain-relief for each electrode using microcoils and a custom coiled cable was employed at the dural–spinous process anchor points to accommodate the increased micro- and macro-motions of the porcine spinal cord. The results from IHC demonstrate that this configuration effectively decouples the implant from spinal movement, mimicking untethered electrode implantation, that confined the chronic foreign-body reactivity to a narrow ~200 µm radius around each electrode (Extended Fig. 5).

The specificity and variety of movements generated by ISMS at low stimulation amplitudes are critical for restoring functional over ground walking. In neural interfaces for the brain, penetrating electrodes are used for both recording and stimulation to achieve the spatial selectivity required to access distinct neural populations, whereas surface electrodes provide broader and less specific activation. To date, spinal cord neuromodulation has relied almost exclusively on surface-based approaches such as eSCS, largely due to the substantial engineering challenges associated with penetrating interfaces in a structure that undergoes large ROM. Our results suggest that overcoming these challenges enables access to more selective spinal motor circuitry, supporting the generation of diverse and functionally relevant movements that may not be achievable with surface stimulation alone. While eSCS can benefit individuals with SCI gain functions such as blood pressure regulation and bladder function by facilitating broad activation, ISMS's activation specificity has the distinct potential to restore functional, adaptive, weight-bearing, over ground walking in individuals with severe SCI.

Conclusion and Future Perspectives

In this study, we demonstrated the first fully implantable, wirelessly controlled ISMS system capable of targeting the entire lumbar enlargement in a clinically relevant large-animal model. Acute implantation and functionality testing confirmed graded movements across the hindlimb joints, and short-term chronic implants (8–14 days) produced a FBR that was confined to a ~200 μm radius, comparable to, or smaller than, that reported for conventional penetrating electrodes. By integrating laser-microfabricated microwire leads with strain-relief mechanisms, the developed ISMS system tolerated substantial spinal motion and maintained electrode positioning. Transient postoperative recovery trends appeared within the first two weeks post-surgery, and all the implanted electrodes (55) remained in place without pronounced migration. The highly localized scar tissue around implanted electrodes suggests that common features of spinal surgical interventions (e.g., epidural hematoma) rather than intraspinal electrode implantation would need to be managed. As a proof-of-concept feasibility study, the chronic implantation periods were intentionally limited. These early time points were selected to capture the period of highest risk for mechanical dislodgement and acute foreign body responses in a large animal model with spine and spinal cord dimensions similar to those of humans. Building on the findings of this study, longer-term studies will be performed to fully characterize mechanical durability, electrochemical performance, and chronic tissue response over extended implantation periods.

Future work will focus on incorporating high-resolution pre-surgical MRI to tailor array geometry to individual spinal cord anatomy and optimize insertion trajectories. Performing serial post-operative MRI for monitoring and quantifying epidural hematoma or spinal cord edema to allow timely interventions. Use of ultra–thin, flexible thin-film electrodes can occupy less intradural volume and may further reduce glial encapsulation of implanted electrodes. While multisite electrodes have been previously tested in ISMS[21,24,29,50], we used single site electrodes as the focus of this study was to evaluate the feasibility and stability of the ISMS device. Incorporation of multi-site, multilayer stimulation pads on each shank can enhance the targeting capacity of distinct locomotor-related networks along the rostrocaudal and dorsoventral axes of the lumbar enlargement[101]. Developing image-guided, robot-assisted implantation can further increase targeting accuracy and reproducibility[107,108]. Evaluating the motor responses produced by ISMS in pigs in long-term studies and performing continuous stimulation paradigms will demonstrate long-term implant stability, fatigue-resistance and capacity to induce overground walking as demonstrated in cats[15,34] .

Collectively, these enhancements will pave the way for a human-compatible ISMS implant—offering high-selectivity, fatigue-resistance and the ability to restore standing and walking in persons with paraplegia due to complete SCI.

Limitations

This study was designed as an early-stage proof-of-concept to evaluate initial device feasibility, electrode stability, and early tissue response. It provided critical outcomes that inform the design of a long-term study in adult Yucatan minipigs (stable weight of ~50kg), an animal model most suitable for such studies. Given the proof-of-concept nature of the study, a few limitations are identified. First, the number of animals utilized and the duration of in vivo testing were modest due to the logistical constraints of studies in domestic pigs that grow at a rate of 5kg per week. Moreover, since the study was not designed to follow animals through to complete behavioural recovery, the partial neurological recovery observed should not be interpreted as a definitive ceiling on achievable function, but rather as motivation to refine surgical techniques and peri-operative management, and inform the design of a long-term study. Second, the study did not include a sham-operated control group or serial in vivo MRI, which limits our ability to directly dissociate the effects of laminectomy, durotomy and postoperative edema or hematoma from those of the penetrating electrodes themselves. Finally, the present device and experimental design were optimized for early feasibility and stability. Longer term studies will be

needed to assess mechanical durability, electrochemical performance, and functional restoration.

Methods

Ethical Approval

All procedures including the experimental design, conduct, and reporting of this animal study were approved by the University of Alberta Animal Care and Use Committee and fully conform to the ARRIVE guidelines. All methods were performed in accordance with the relevant guidelines and regulations.

Electrode Fabrication

Electrodes were fabricated from 50 µm diameter Pt-Ir (80%:20%) microwires (California Fine Wire, USA) insulated with 4 µm polyimide. Wires were cut into 15 cm lengths and secured into custom-made acrylic fixtures. The distal and proximal ends of the electrodes were de-insulation (~500 µm length) via laser microfabrication using either nanosecond pulses (KrF excimer laser, COMPex 110, Coherent, USA) or femtosecond pulses (1030 nm, with automated harmonics generator, Carbide, Optec, Belgium). Using the nanosecond laser, the rectangular variable aperture sizes were adjusted to cover the 500 µm de-insulation length in each pulse; 10 pulses (10 Hz, 20 ns, 248 nm, 150 mJ, 75% attenuation) were found sufficient to remove the insulation without damaging the underlying metal layer. Whereas in the case of the femtosecond laser (spot size ~6 µm), 100 lines, 5 µm apart, were scanned perpendicular to the longitudinal axis of the microwire (10 mm/s, 60 kHz, 243 fs, 343 nm, 0.7 µJ). The acrylic blocks were rotated 4 times to ensure de-insulation of the entire circumference of the electrode for both lasers.

Electrode tips were beveled at a 15° angle at the distal end (tip) using a electrode beveler (BV-10, Sutter, CA, USA) or laser cutting. Electrodes were then ultrasonically cleaned in Alconox detergent for 30 minutes, rinsed in deionized water for an additional 30 minutes, and sterilized using 70% ethanol. Subsequently, electrodes were coated electrochemically with poly(3,4-ethylenedioxythiophene) (PEDOT, 200 mC/cm^2) to standardize the geometric surface area (GSA).

The length of electrodes in an array depended on the electrode number and its rostrocaudal location in the array with electrodes being 5, 4.8, 4.6, 4.4, 4.2, 4.0, and 3.8 mm long moving from the rostral to caudal direction. These lengths were defined based on anatomical measurements of pig lumbar spinal cord[42].

Electrochemical Tests and Cleaning Protocol

After removal of the insulation by laser ablation, electrodes were cleaned in 0.01 M PBS (pH 7.4) at room temperature, using an Ag/AgCl reference

electrode. Cyclic voltammograms (CVs) at scan rates of 50 mV s^{-1} and 50 V s^{-1} and EIS (explained below) were obtained prior to electrode cleaning. Next, a single oxidative CV sweep at 4 mV s^{-1} was performed between +1.0 V and +2.0 V (returning to +1.0 V) to enter the oxygen-evolution region and oxidatively strip any residual organic deposits[109]. CVs were again recorded at 50 mV s^{-1} and 50 V s^{-1} and EIS post-cleaning. CV and EIS were performed for quality assurance before and after the electrochemical cleaning protocol.

Electrochemical characterization of the implantable electrodes was carried out both in vitro and in vivo to quantify impedance, charge storage, and charge-injection capabilities. In vitro measurements were performed at room temperature in Dulbecco's PBS (Sigma-Aldrich, MO, USA) using a MET16 potentiostat (Sigenics Inc., IL, USA) inside a Faraday cage. A de-insulated stainless-steel counter electrode (Cooner AS632; 3–5 cm exposed; Cooner Wire Company, CA, USA) and an Ag/AgCl reference electrode were used in a three-electrode setup for in vitro measurements. EIS was carried out by applying a 10 mV rms sinusoidal perturbation and sweeping frequencies from 0.1 Hz to 100 kHz to obtain both magnitude and phase spectra. CV was performed within the water-window of Pt–Ir (–0.6 V to +0.8 V versus Ag/AgCl); after 13 preliminary cycles, the final three scans were integrated to compute the cathodal charge storage capacity (CSCc), which was then normalized to the geometric surface area of the electrode. Voltage transient analysis employed cathodic-leading, biphasic current pulses (200 µs per phase, 100 µs interphase) with amplitudes increased in 25 µA increments until the maximum cathodic polarization ($E_{mc} \approx -0.6$ V)[55] was reached. The charge injection capacity (Q_{inj}) was determined by normalizing the delivered charge at E_{mc} to electrode area.

In vivo electrochemical testing was conducted acutely in a domestic pig model (n = 4) following implantation (see Surgical Procedure, Section F). A two-electrode configuration was adopted, in which the implanted electrode acted as the working electrode and a large-gauge needle inserted into the paraspinal muscle served as the counter. Impedance and voltage-transient protocols were identical to those used in vitro, enabling direct comparison of electrochemical performance under physiological conditions.

Microcoil Fabrication

Microcoils for strain relief were fabricated by winding 80:20 Pt–Ir microwires (California Fine Wire, USA) of 25 µm outer diameter (including ~4 µm of polyimide insulation) onto 125 µm-diameter tungsten mandrels using a custom coiling apparatus under an optical microscope. The microwires were cut to 25 mm total length, and a length of 7 mm was coiled. Two microcoil geometries were produced: a no-pitch configuration (≈ 40 turns mm^{-1}) and a spaced-pitch configuration with 30–40 µm inter-

turn spacing (≈ 25–30 turns mm^{-1}). The coiled segment (made from already insulated microwires) was further dip-coated in PDMS at either 5 mm/min or 20 mm/min pull out speeds using a KSV NIMA Small Dip Coater (Multi-Vessel Systems, Phoenix, AZ, USA). Microcoils were then cured at 80 °C for 10 min to cure the PDMS insulation. After curing, the uncoiled distal segment of each microwire (≈1 mm long) was de-insulated over a 300 µm length using femtosecond laser ablation as explained in the Electrode Fabrication section above. This exposed the Pt–Ir metal core and prepared the microcoil tip for orthogonal joining to the proximal end of the electrodes at about 90° angle using laser welding.

Laser Micro welding

Electrode–microcoil assemblies were joined by laser welding using a fiber laser working station (7800 series; LaserStar Technologies, FL, USA) equipped with micro motioning platform. Prior to welding, both the de-insulated microcoil tip and the electrode tip were cleaned in acetone and isopropanol, then clamped between two 4 mm-thick, 10 mm-diameter PDMS disks for handling and protection during alignment. The 25 µm Pt–Ir microwire was oriented orthogonally atop the electrode tip to form a 90° junction[66]. Welding parameters were optimized by testing pulse energies from 100–600 mJ, pulse widths of 0.5, 1, and 2 ms, translating into peak powers between 75 W and 300 W, with powers below 75 W failing to achieve metal fusion. Mechanical integrity of each joint was assessed via joint breakage force testing on a custom made uniaxial tensile testing machine occupied with a 100 g load cell (GSO100, TMO-2 signal conditioner; Transducer Techniques, CA, USA). Microstructural and compositional analyses were performed by SEM with energy-dispersive X-ray spectroscopy using a Phenom XL Desktop SEM (Nanoscience Instruments, PA, USA) to confirm oxide-free fusion, and cross-sectional inspection via focused ion beam SEM (Helios Hydra Plasma; ThermoFisher Scientific, OR, USA) to evaluate pore distribution and impurity inclusion. Finally, each weld site was encapsulated by PDMS drop-casting and cured at 120 °C with low airflow using a handheld heat gun.

Coiled Cable Assembly

The tips of electrodes connected to the 25 µm microwire leads with microcoils were inserted into two parallel medical grade Silastic tubes (ID: 0.5, OD 0.9 mm, Dow Corning, MI, USA). Seven electrodes were inserted per tube spaced 6 mm apart for bilateral spinal cord implantation (Fig. 1a, 1b, Fig. 3a), and the tubes were affixed to a transparent support sheet to facilitate handling. The proximal end of the 25µm microwire leads (~20 cm) was briefly wetted with deionized water and gathered by gentle compression with gloved fingers to make a bundle of the 14 microwires. The microwire proximal ends were then de-insulated and soldered to a 75 µm Pt–Ir lead to allow threading of the bundle into silastic tubing (10 cm long,

0.9 mm OD). The distal end of the tube containing the microwire bundles was clamped to a 200 µm tungsten rod using micro–alligator clips, then the tube was stretched to ~20 cm, helically wrapped around the tungsten rod (~25 turns/cm), and gently released applying pre-strained compression to the helical part (Fig. 3a). Finally, the tube with the helically coiled microwire bundle was infused with PDMS via a 30-gauge needle using a syringe pump at 1 µl/min and cured at 60 °C overnight. After curing, the proximal ends of the individual microwires were soldered to the male contacts of two extension cables (Medtronic 37081) using low-temperature, lead-free solder and a 200 µm soldering tip. The junction was seated within a custom grommet, 3D-printed from BioMed Elastic 50 A resin (Formlabs, MA, USA) and the cavity was backfilled with medical-grade flowable silicone (DOWSIL™ 734 Flowable RTV Sealant; Dow Silicones Corporation; MI, USA). Assemblies were placed on a level surface and allowed to cure overnight, ensuring a leak-proof seal and strain-relieved connection.

Mechanical Characterization

Mechanical characterization of microcoils and coiled cables was performed by uniaxial tensile testing on strain-gauge load cells (GSO10 for microcoils; GSO100 for coiled cables; both interfaced to a TMO-2 signal conditioner; Transducer Techniques, CA, USA). Each load cell was calibrated against ten known 3D-printed masses, yielding a perfect linear response ($R^2 = 1.00$). Microcoils (initial length ≈ 7 mm) and coiled cables (100 mm length) were preloaded to remove slack and then stretched at a constant extension rate of 500 µm s^{-1} using a custom Raspberry Pi–controlled linear actuator. Six designs were evaluated, with at least four replicates per design: no pitch/no coating, pitched/no coating, pitched/coated at 5 mm/min or 20 mm/min, and no pitch/coated at 5 mm/min or 20 mm/min. Tests were conducted at room temperature. Microcoils and coiled cables were extended to 400% and 40% strain, respectively, capturing both elastic and plastic behavior. Load–displacement data were recorded on a Tektronix oscilloscope (MDO3014; 100 000 data points) and used to extract elastic modulus, yield force, and ultimate tensile force.

Weld joint breakage forces (JBF) were measured on de-insulated 25 µm and 50 µm microwires welded orthogonally at 90-degree angle (1 cm length; n = 4 per each parameter set; Extended Fig. 3c). In these tests, the 50 µm-diameter end was clamped to the load cell and the 25 µm end to the moving stage; tension was increased until junction failure. Data acquisition and analysis followed the same protocol as for microcoils and cables. The mechanical properties of isolated 25 µm were performed on 2cm long de-insulated microwires.

Implantable Wireless Stimulator

The wireless stimulation modules were assembled at the Laboratory of Neural Prosthetic Research (LNPR) at the Illinois Institute of Technology (IIT, Chicago, IL, USA). Each module contained a miniature application-specific integrated circuit (ASIC) designed by Sigenics, Inc. (Chicago, IL, USA). The stimulator assembly included an external platinum reference/counter electrode with a geometric surface area of 105 mm^2. The electronics were encapsulated within a cylindrical casing (approximately 3 cm in diameter and 7 mm thick) fabricated using filament-based 3D printing with medical-grade MPU-100 polymer (Carbon, Inc., Redwood City, CA, USA). To ensure electrical insulation and mechanical stabilization, the interior of the medical grade casing was filled with a DOWSIL 3140 RTV coating to provide insulation to the electronic components. The internal components of the wireless stimulation module are shown in Extended figure 1c and 1d.

The custom ASIC in the stimulation module enabled wireless power and data transmission through two coils: one embedded within the module itself and the other part of an extracorporeal telemetry controller unit, positioned 5–10 cm away from the implanted stimulator and external to the animal. Power and data transmission occurred via a 4.8 MHz wireless magnetic link through the TC's extracorporeal coil. Wireless communication used ASCII-encoded command structures, allowing for control of stimulation parameters and real-time monitoring of device status via reverse telemetry. The reverse telemetry function provided electrode voltage transient measurements during constant-current pulsing, as previously described[110]. These measurements capture the electrode's maximum cathodic excursion and driving voltage, both of which are crucial for ensuring that the electrodes can deliver charge safely without exceeding the potential limits associated with water electrolysis and preventing noxious electrochemical reactions that could damage the electrode or tissue.

The system was employed to deliver charge-balanced, cathodic-first biphasic asymmetric pulses. Stimulation parameters, including cathodic current amplitude, pulse width, interphase intervals, and pulse frequency, were configured through a custom MATLAB-based graphical user interface, which communicated with the transmitter coil via a serial USB connection.

Surgical Implantation Procedure

All acute procedures were performed under aseptic surgical conditions, while recovery procedures were performed under sterile surgical conditions. We assessed surgical feasibility (n = 4; 52.3 ± 7.1 kg), functional performance (n = 6; 51.5 ± 4.7 kg) and chronic safety (n = 4; 46.6 ± 2.6 kg) of the array in female domestic pigs. Female domestic pigs weighing 45–55 kg were selected because their lumbosacral spinal cord and vertebral canal dimensions closely approximate those of adult humans[42,43],

while still permitting safe anaesthesia, surgical exposure, and postoperative handling. The target sample size for chronic implantation (4 pigs) was chosen a priori to balance the need for repeated histological and imaging assessments with the logistical constraints of neurosurgical research in domestic pigs that grow at a rate of 5kg per week. The present study was designed as an early feasibility and device stability study. One animal (P4) was excluded from safety assessment due to additional compilations occurring post-surgery such as rectal prolapse (see next section for more detail). For chronic experiments, the complete system was immersed in a cold-sterilization solution for at least 2 hours followed by rinsing in sterile saline for 3 hours.

Pigs were premedicated with intramuscular ketamine (20 mg/kg; 100 mg/mL) and glycopyrrolate (0.01 mg/kg; 0.2 mg/mL). Anesthesia was induced with a brief initial administration of isoflurane (inhalation) and maintained via continuous intravenous infusion of propofol (40–145 µg/kg/min; 10 mg/mL), remifentanil (0.03–0.14 µg/kg/min; 1 mg/mL), lidocaine (1 mg/kg/hr; 20 mg/mL), and dexmedetomidine (0.2 µg/kg/hr; 0.5 mg/mL) using syringe pumps (Harvard Apparatus, 702208, MA, USA).

Animals were positioned prone on a custom surgical table with their hindlimbs suspended to maintain neutral spinal alignment during intraspinal electrode implantation. A midline skin incision was carried down through subcutaneous tissue to expose the laminae of L3–L6 vertebrae. Topical 2% lidocaine was applied to the exposed periosteum before performing complete laminectomies of L4 and L5 and partial removal of the L3 and L6 laminae to reveal the lumbar enlargement. The dura mater was then opened longitudinally, tented, and intraoperative ultrasound (Sonosite PX, Fujifilm SonoSite, Bothell, WA, USA) was used to verify correct spinal alignment and confirm absence of cord rotation both before and after durotomy (Extended Fig. 4a).

Using a surgical microscope and with real-time ultrasound guidance, electrodes were inserted manually with tips targeting specific locations within the ventral horn to achieve hip flexion, knee extension, ankle flexion, ankle extension, hip extension, and knee flexion, proceeding from L4 spinal segment caudally to S1/S2 on both the left and right sides. A PDMS tab was sutured to the dentate ligaments at the L3 level to anchor the array to the spinal cord (at the transition point of the 14 lead wires to the coiled cable). In chronic studies (animals P2–P4), the PDMS tab was removed and instead the coiled cable was sutured directly to the dura mater at its exit point, leaving a short length of slack in the intradural space. The dural incision was closed with interrupted 8-0 Prolene sutures. In P3 and P4, a duraplasty was performed by suturing a piece of dural substitute (~ 15 mm × 90 mm;

Gore Preclude) to the dural margins with 8-0 Prolene to expand the subdural space.

The surgical wound was then sutured shut in layers and a subcutaneous pocket was created in the caudal thoracic region to house the stimulator. The male ends of two Medtronic extension cables were tunneled via a trocar to this pocket, where they connected and secured with screws to the female connectors of the other extension cables connected to the coiled cable.

Post-operative Animal Care

Post-surgery pigs were housed in clean pens lined with padded mattresses to prevent self-injury and protect surgical sites. Animals received analgesics, antibiotics, hydration support, nutritional care, wound management, and routine monitoring detailed as follows:

Vital Sign and Clinical Monitoring Timeline:

Vital signs including heart rate, respiratory rate, rectal temperature, hydration status, food and water intake, mobility, defecation, urination frequency, and general demeanor were closely monitored at specific intervals post-surgery. The animals were monitored hourly for the first 24 hours post-surgery, followed by monitoring every 4 hours during the subsequent 24 hours. Monitoring was conducted every 6 hours over the ensuing 48 hours, every 8 hours over the subsequent 48 hours, and at least twice daily thereafter. Discomfort and pain indicators were assessed at each monitoring time point to ensure optimal comfort levels during recovery. Additional parameters evaluated included posture, responsiveness, vocalization, grooming, and wound appearance.

Analgesia and Antibiotic Administration:

Animals were administered analgesics immediately following surgery and continued postoperatively. Hydromorphone (0.05 mg/kg intravenous every 6–8 hours) or slow release buprenorphine administered subcutaneously (0.1-0.18 mg/kg every 72 hours) was provided during the initial 72 hours post-surgery. Tramadol (5 mg/kg orally, twice daily) and meloxicam (0.4 mg/kg orally, once daily) were given regularly for two weeks postoperatively. Cefazolin (25 mg/kg intravenously, every 12 hours) was administered during the first three postoperative days, followed by oral cephalexin (20 mg/kg twice daily) for 10–14 days.

Hydration and Nutritional Support:

During the first 24 hours post-procedure, 50 mL of Lactated Ringer’s solution was administered hourly via the auricular catheter at a slow, controlled rate to maintain adequate hydration. Oral hydration was supported with syringe-administered water or diluted electrolyte drinks (e.g., Gatorade) to motivate the animals to drink. Nutritional intake was

closely monitored. Dry feed was offered initially by bringing the food bowl directly to the animal. If animals refused the dry feed, water was added to create a moist food slurry and then re-offered orally. Stool consistency was monitored, and laxatives (Lactulose) were administered orally if needed.

Routine Wound Management and Skin Care:

Surgical dressings (Tegaderm and sterile gauze) were inspected daily and replaced if any contamination was noted. Prophylactic zinc-oxide cream was applied to pressure-prone sites—including hocks, elbows, hips, and groin to prevent pressure injuries. Incision regions were examined at regular intervals and treated with topical antibiotic ointment (Polysporin).

Mobility and Physical Rehabilitation:

During the first three postoperative days, animals were manually repositioned every 4–6 hours, then every 8–12 hours thereafter. Daily passive range-of-motion exercises—including hip, knee, and ankle flexion and extension—were performed to prevent contractures and preserve joint mobility. For animal P4, an overhead sling was initially used to offload the limbs, but it induced spinal hyperextension and increased bladder pressure, leading to urinary dribbling. Sling use was therefore discontinued, and caregivers instead provided manual lift-assisted standing and ambulation to support weight bearing, promote circulation, and minimize complications from prolonged recumbency

Rectal Prolapse and Complication Management:

Rectal prolapse was noted in two animals (P1 and P4). In P1, prolapse occurred on post-operative day 7—one day before the planned day 8 euthanasia—and the animal was humanely euthanized immediately upon diagnosis. In P4, prolapse presented on day 1 and was managed under intramuscular sedation with ketamine (9.3 mg/kg) and glycopyrrolate (0.05 mg/kg). A circumferential purse-string suture (2-0 polypropylene) was placed at the anal margin to reduce and secure the prolapse, and 1 mL of 2 % lidocaine was then infiltrated around the perianal tissues for local analgesia. Following recovery from ketamine, P4 exhibited transient exaggerated body-twisting movements for nearly 2 hours due to disorientation while recovering from the effect of ketamine. This unfortunately dislodged the electrode array at a time post-surgery during which the implants are at the highest risk of displacement. Nonetheless, the animal was monitored closely thereafter to confirm prolapse reduction, ensure comfort, and detect any recurrence. No further episodes of rectal prolapse occurred through the end of the experiment. On postoperative day 21 in this same animal, the stimulator showed signs of causing internal tissue compression leading to a deep tissue injury that caused substantial swelling. The stimulator was therefore explanted under general anesthesia induced with intramuscular ketamine (12.3 mL; 100 mg/mL),

dexmedetomidine (2mL, 0.5 mg/mL), and subcutaneous meloxicam (4.3 mL of 5 mg/mL). A 5 cm longitudinal skin incision was made over the original implant site, revealing a yellow fibrinous layer in the subcutaneous pocket, which was debrided. The device lead was transected at its exit point, and the stimulator body was removed intact. The pocket was then irrigated with povidone–iodine solution, a closed-suction drain was placed, and the wound was closed in two layers: deep fascial closure with interrupted 2-0 Vicryl sutures, followed by skin closure with simple interrupted sutures.

While P4 was not included in the immunohistochemical results, it provided critical understanding regarding the frequency of prolapse complications in pigs, internal tissue compression by the stimulator which necessitates placing the stimulator closer to the abdominal region instead of the back. It also confirmed what we had known for work in other species that excessive twisting movements soon after surgery can dislodge the ISMS implant. Therefore, strict protocols for reducing these twisting movements are necessary in large animals recovering from the surgical procedure.

Euthanasia, Perfusion and Immunohistochemistry

At the conclusion of the experimental period in acute and short-term chronic procedures, animals were deeply anesthetized, and euthanasia was induced by slow intravenous infusion of sodium pentobarbital (Euthanyl, 100 mg/kg) via a jugular catheter. Immediately thereafter, 4 L of physiological saline followed by 8 L of 4% paraformaldehyde were infused through the carotid artery and drained via the hepatic vein. To accelerate flow, small incisions were made in the liver and suction wands were applied while a portable fume extractor (Sentry Air Systems, TX, USA) removed formaldehyde vapors. The spinal cord (segments L2–S2) and adjacent tissues were then dissected en bloc and post-fixed in 4% paraformaldehyde at 4 °C for 24–48 hours, during which post-mortem MRI and X-ray imaging were performed. Finally, samples were cryoprotected by immersion in 10% sucrose in PB for 72 hours, followed by 30% sucrose in PB at 4 °C for a minimum of 1 week.

Tissue Block Preparation and Sectioning:

Post-mortem MRI guided the dissection of 10–15 mm tissue blocks containing both implantation sites and rostral control regions. These blocks were embedded in optimal cutting temperature (OCT) compound, snap-frozen on isopentane, and stored at –80 °C. Serial transverse and coronal sections (20 µm thickness) were cut on a cryostat. Three to five sections were mounted per SuperFrost Plus slide, air-dried for 30 min at room temperature, and then returned to –80 °C. Each set of ten slides comprised 30-50 serial sections spanning 600 µm to 1 mm of the lumbar enlargement. One slide per set of 10 was stained with Harris hematoxylin & eosin (H&E),

which served to verify electrode tracks and identify tissue disruption from pial incisions or electrode insertion.

Spinal Cord Immunohistochemistry:

Sections at 200 µm intervals underwent H&E staining to assess electrode tracks and glial scar. Immunohistochemistry (IHC) was performed on sections that neighbored electrode tracks identified by H&E staining. Slides were stained with myelin-based protein (Bio-Rad as-82-87, 1:2000) (MBP) and neurofilament (Millipore N0142, 1:3000) (NF), CD 68 (Abcam ab31630, 1:2000) and ionized calcium binding adapter molecule 1 (Iba1) (Abcam ab153696, 1:500), or glial fibrillary acidic protein (GFAP) (DAKO Z0334, 1:500) and NeuN (Millipore ABN90P, 1:1000). All slides were also stained with 4′,6-diamidino-2-phenylindole (DAPI) that was in the mounting media (Vectashield). Secondary antibodies used included Alexa Fluor Goat anti Mouse 488 (Invitrogen- A21121, 1:400), Alexa Fluor Goat anti Rat 568 (Invitrogen- A11077, 1:400), Alexa Fluor Goat anti Rabbit 568 (Invitrogen- A11036, 1:400), Alexa Fluor Goat anti Rabbit 488 (Invitrogen- A11037, 1:400), and Alexa Fluor Goat anti Guinea Pig 568 (Invitrogen- A11075, 1:400). The IHC procedure involved 5-minute rinses in PBS with 4% Triton x-100 (PBS Tx) and PBS. Tissue was then incubated overnight at 4°C in a blocking solution made up of 10% normal goat serum and PBS Tx. The next day the primary antibody was diluted with the same blocking solution and was incubated at 4°C overnight. Day 3 involved rinses in PBS Tx and PBS, a 2 hour incubation at room temperature in secondary antibody diluted in blocking solution. Secondary antibody incubation and all following steps were done in the dark to prevent the loss of fluorescent signal. Tissue was then rinsed in PBS, followed by rinsing for 10 minutes in cupric sulphate, and then rinsed again in PBS. Slides were covered slipped using Vectashield mounting media with DAPI, and were left in a dark cupboard to dry overnight and subsequently transferred to the -20°C freezer.

Electrode Immunostaining:

Immediately before freezing, explanted electrodes were transferred to vial tubes, submerged in PBS, and subsequently placed into cell culture wells for immunolabeling. Nuclei were counterstained with Hoechst, microglia labeled with Iba1, neuronal somata with NeuN, and macrophages/microglia with Iba1. All staining steps were performed under fully hydrated conditions, and specimens were imaged using a confocal microscope (Leica TSC SPE, HE, Germany).

Imaging and Quantitative Analysis:

Brightfield images were captured using a Leica DM4000 microscope (Leica Microsystems, Wetzlar, Germany). Coronal sections were digitized in their entirety at 20× magnification on a Zeiss Axioscan. Z1 high-throughput slide scanner (Carl Zeiss AG, Oberkochen, Germany). Quantitative assessment of

marker distribution surrounding electrode tracks was achieved through ring-based fluorescence intensity analysis implemented in a custom automated Python script. For higher-resolution analysis, confocal micrographs were acquired on a Leica TSC SPE system, while widefield epifluorescence images were obtained on a Leica THUNDER Deconvolution microscope, employing instant computational clearing to remove out-of-focus background.

All coronal section images were initially grouped by tissue type (WM vs. GM) and staining combination, which included three fluorophores imaged across three channels: DAPI in the blue channel, and two antibodies in the red and green channels. For each staining combination within either the WM or GM, mean fluorescence intensities were calculated in 7.5 µm-wide rings centered on the area of damage (defined manually), extending radially up to 750 µm from the center.

A baseline for each channel was established as the average intensity of the outermost ten rings (675–750 µm from the center of the void created by each electrode), and all intensities were normalized relative to this baseline. Raw and normalized intensity data for the three channels were stored in CSV files for each image. From each normalized intensity profile, the radius at peak normalized intensity and the maximum normalized value were identified. The mean ± SD of intensity values across all profiles within the same antibody channel and tissue type (WM, GM) were calculated for both raw and normalized intensities for each animal. Finally, these values were averaged across the 3 animals to obtain mean ± standard error values for both raw and normalized intensity profiles across a 1.5 mm radius surrounding the electrodes in both WM and GM.

MRI, X-ray and ultrasound

We performed real-time ultrasound imaging guidance during electrode implantation using a Sonosite PX system (Fujifilm SonoSite, Bothell, WA, USA) equipped with an L19-5 linear probe (19–5 MHz) set to the “Nerve Exam” preset, and scanned at depths ranging from 1.8 to 3.7 cm. Following euthanasia, the excised spinal cord (without surrounding bone) was immersed in Fluorinert (Sigma Aldrich, MO, USA) to minimize susceptibility artifacts, and imaged using MRI. Two systems were employed: a 4.7 T Varian scanner (Varian, CA, USA) with a spin-echo sequence yielding 0.063 × 0.063 × 1 mm voxel resolution, and a Bruker BioSpec 3 T preclinical scanner (Bruker, Germany) using a multi-echo 3D or T1–TurboRARE providing 0.125 × 0.625 × 1 mm resolution. These MRI protocols provided clear contrast between GM and WM that assisted in the localization of electrode tips within the cord. High-resolution micro–X-ray microscopy was also performed on a ZEISS Xradia Versa 620 system using both 0.4× and

4× objectives, yielding enhanced contrast images of the metal electrode array in three dimensions.

Kinematic and Isometric Force Evaluation

In acute experiments, reflective markers were affixed to the iliac crest, hip, knee, ankle and metatarsophalangeal joints using double-sided tapes, and movements were recorded in the sagittal plane using a camera placed orthogonally to the sagittal plane. For knee extension and hip flexion movements, the knee and hip joints were pre-flexed and pre-extended, respectively, with a 1–2 lb hanging weight and pulley system[46,49]. Marker centroids were extracted via threshold-based detection in custom Python scripts. When illumination was insufficient, marker less tracking with DeepLabCut was used. Both methods were able to identify the centre point of the markers and extract their coordinates. Joint angles were computed for three repetitions per movement, averaged within each animal, and then pooled to yield mean ± SEM. Kinematics were assessed over stimulation amplitudes of 25–300 µA, with statistical comparisons at 100, 200, and 300 µA. Range of motion for hip, knee and ankle joints at 100, 200, and 300 µA was calculated by averaging across repetitions and animals. In chronic experiments, we avoided physical markers to maintain sterility during the implantation surgery. Movement type evoked with a maximum stimulation amplitude of 125 µA was documented for each electrode.

Isometric joint forces were measured with a 150 lb load cell (Interface Inc., Scottsdale, AZ, USA) connected to custom amplifiers and digitized on an oscilloscope (Tektronix MDO3014). For each movement, isometric forces were recorded three times at each stimulation amplitude (25–300 µA range). The peak force per movement type from each trial was normalized within each animal to that movement's maximum isometric force. The average normalized force values were calculated for each movement type per stimulation amplitude for each animal, and then averaged across animals. Recruitment curves were generated by plotting these averaged normalized forces against stimulation amplitude.

Statistical Analysis

Statistical analyses were performed in GraphPad Prism (GraphPad Software Inc., San Diego, CA, USA). Data normality was assessed by the Shapiro–Wilk test. Microcoil mechanical properties (yield strain and yield force), electrochemical impedance spectroscopy parameters (impedance magnitude and phase angle), and cathodic charge storage capacity (CSCc) were compared by one-way ANOVA with Bonferroni correction. Charge-injection limit (Q_{inj}) was compared between in vitro and in vivo

electrodes using the nonparametric Mann–Whitney U test. Sigmoidal four-parameter logistic regression of mean normalized force values was used to extract the Hill slope and recruitment steepness. Immunofluorescence metrics (maximum intensity and radius at peak) across antibodies and spinal cord regions (gray versus white matter), joint breakage forces across laser-welding energy and pulse-width conditions, and maximum cathodic excursion (E_{mc}) across stimulation amplitudes and experimental conditions (uncleaned in vitro, cleaned in vitro, in vivo) were evaluated by two-way ANOVA with Bonferroni post hoc correction. Significance value was set at $p < 0.05$. Data are reported as mean ± standard deviation unless otherwise indicated.

Acknowledgments

The authors would like to acknowledge Dr. Aaron Huckely for assistance with some of the surgical procedures; Katie-Marie Buswell-Zuk and Ryan Edgar, and Katie Rousu for surgical monitoring and maintenance of anesthesia at the Ray Rajotte Surgical Medical Research Institute; Peter Seres for MRI scans; David Roszko, Michel Gautier and Rod Gramlich for technical assistance with electromechanical devices; and Dr. Leanne Paetkau, Dr. Nathan Bosvik and Dr. Isabelle Gauthier for veterinary support.

Funding Declaration

This work was funded in part by the US Department of Defense Congressionally-directed Medical Research Program—Spinal Cord Injury Research Program, Canadian Institutes of Health Research, Canada Foundation for Innovation, Prairies Economic Development Canada, University of Alberta Hospital Foundation, and Brain Canada Foundation. SM was supported by a Faculty of Medicine and Dentistry Dean's Doctoral Scholarship, a 75th Anniversary Scholarship, an Alberta Graduate Excellence Studentship and an Alberta Innovates Graduate Studentship. CLO was supported by an Alberta Graduate Excellence Studentship and a Natural Science and Engineering Research Council Graduate Scholarship. AA was supported by a 75th Anniversary Faculty of Medicine and Dentistry Graduate Student Award and a Mary Louise Imrie Graduate Student Award. VKM is a Canada Research Chair (Tier 1) in Functional Restoration.

References

1. Ding, W. *et al.* Spinal cord injury: the global incidence, prevalence, and disability from the global burden of disease study 2019. *Spine* **47**, 1532–1540 (2022).

2. Lu, Y. *et al.* Global incidence and characteristics of spinal cord injury since 2000–2021: a systematic review and meta-analysis. *BMC medicine* **22**, 285 (2024).
3. National Spinal Cord Injury Statistical Center. Traumatic spinal cord injury facts and figures at a glance. *Birmingham, AL: University of Alabama at Birmingham* https://msktc.org/sites/default/files/Facts-and-Figures-2024-Eng-508.pdf (2024).
4. Dimitrijevic, M. R., Gerasimenko, Y. & Pinter, M. M. Evidence for a spinal central pattern generator in humans a. *Annals of the New York Academy of Sciences* **860**, 360–376 (1998).
5. Angeli, C. A. *et al.* Recovery of over-ground walking after chronic motor complete spinal cord injury. *New England Journal of Medicine* **379**, 1244–1250 (2018).
6. Harkema, S. *et al.* Effect of epidural stimulation of the lumbosacral spinal cord on voluntary movement, standing, and assisted stepping after motor complete paraplegia: a case study. *The Lancet* **377**, 1938–1947 (2011).
7. Gill, M. L. *et al.* Neuromodulation of lumbosacral spinal networks enables independent stepping after complete paraplegia. *Nature medicine* **24**, 1677–1682 (2018).
8. Rowald, A. *et al.* Activity-dependent spinal cord neuromodulation rapidly restores trunk and leg motor functions after complete paralysis. *Nature medicine* **28**, 260–271 (2022).

9. Wagner, F. B. *et al.* Targeted neurotechnology restores walking in humans with spinal cord injury. *Nature* **563**, 65–71 (2018).
10. Mesbah, S. *et al.* Neuroanatomical mapping of the lumbosacral spinal cord in individuals with chronic spinal cord injury. *Brain Communications* **5**, fcac330 (2023).
11. Chalif, J. *et al.* Epidural spinal cord stimulation for spinal cord injury in humans: a systematic review. *Journal of Clinical Medicine* **13**, 1090 (2024).
12. Mushahwar, V. K. & Horch, K. W. Selective activation of muscle groups in the feline hindlimb through electrical microstimulation of the ventral lumbo-sacral spinal cord. *IEEE Transactions on Rehabilitation Engineering* **8**, 11–21 (2000).
13. Bamford, J., Putman, C. & Mushahwar, V. Intraspinal microstimulation preferentially recruits fatigue-resistant muscle fibres and generates gradual force in rat. *The Journal of physiology* **569**, 873–884 (2005).
14. Saigal, R., Renzi, C. & Mushahwar, V. K. Intraspinal microstimulation generates functional movements after spinal-cord injury. *IEEE Transactions on neural systems and Rehabilitation Engineering* **12**, 430–440 (2004).
15. Holinski, B. *et al.* Intraspinal microstimulation produces over-ground walking in anesthetized cats. *Journal of neural engineering* **13**, 056016 (2016).

16. Hachmann, J. T. *et al.* Large animal model for development of functional restoration paradigms using epidural and intraspinal stimulation. *PLoS One* **8**, e81443 (2013).
17. Dalrymple, A. N. & Mushahwar, V. K. Intelligent control of a spinal prosthesis to restore walking after neural injury: Recent work and future possibilities. *Journal of Medical Robotics Research* **5**, 2041003 (2020).
18. Dalrymple, A. N., Roszko, D. A., Sutton, R. S. & Mushahwar, V. K. Pavlovian control of intraspinal microstimulation to produce over-ground walking. *Journal of neural engineering* **17**, 036002 (2020).
19. Dalrymple, A. N., Everaert, D. G., Hu, D. S. & Mushahwar, V. K. A speed-adaptive intraspinal microstimulation controller to restore weight-bearing stepping in a spinal cord hemisection model. *Journal of neural engineering* **15**, 056023 (2018).
20. Tawakol, O. *et al.* In-vivo testing of a novel wireless intraspinal microstimulation interface for restoration of motor function following spinal cord injury. *Artificial Organs* **48**, 263–273 (2024).
21. Roszko, D. A. *et al.* Laser-microfabricated polymer multielectrodes for intraspinal microstimulation. *IEEE Transactions on Biomedical Engineering* **70**, 354–365 (2022).
22. Tawakol, O. S. M. S. A Wireless Intraspinal Microstimulation Interface for the Recovery of Motor Function Following Spinal Cord Injury. (Illinois: Illinois Institute of Technology, United States, 2024).

23. Lau, B., Guevremont, L. & Mushahwar, V. K. Strategies for generating prolonged functional standing using intramuscular stimulation or intraspinal microstimulation. *IEEE Transactions on Neural Systems and Rehabilitation Engineering* **15**, 273–285 (2007).

24. Snow, S., Horch, K. W. & Mushahwar, V. K. Intraspinal microstimulation using cylindrical multielectrodes. *IEEE transactions on biomedical engineering* **53**, 311–319 (2006).

25. Prochazka, A., Mushahwar, V. & Yakovenko, S. Activation and coordination of spinal motoneuron pools after spinal cord injury. *Progress in Brain Research* **137**, 109–124 (2002).

26. Guevremont, L. *et al.* Locomotor-related networks in the lumbosacral enlargement of the adult spinal cat: activation through intraspinal microstimulation. *IEEE Transactions on neural systems and rehabilitation engineering* **14**, 266–272 (2006).

27. Mushahwar, V., Aoyagi, Y., Stein, R. & Prochazka, A. Movements generated by intraspinal microstimulation in the intermediate gray matter of the anesthetized, decerebrate, and spinal cat. *Canadian journal of physiology and pharmacology* **82**, 702–714 (2004).

28. Zimmermann, J. B., Seki, K. & Jackson, A. Reanimating the arm and hand with intraspinal microstimulation. *Journal of neural engineering* **8**, 054001 (2011).

29. Sharpe, A. N. & Jackson, A. Upper-limb muscle responses to epidural, subdural and intraspinal stimulation of the cervical spinal cord. *Journal of neural engineering* **11**, 016005 (2014).

30. Tao, C. *et al.* Comparative study of intraspinal microstimulation and epidural spinal cord stimulation. in 3795–3798 (IEEE, 2019).

31. Ibáñez, J., Angeli, C. A., Harkema, S. J., Farina, D. & Rejc, E. Recruitment order of motor neurons promoted by epidural stimulation in individuals with spinal cord injury. *Journal of Applied Physiology* **131**, 1100–1110 (2021).

32. Gaunt, R. A., Prochazka, A., Mushahwar, V. K., Guevremont, L. & Ellaway, P. H. Intraspinal microstimulation excites multisegmental sensory afferents at lower stimulus levels than local α-motoneuron responses. *Journal of neurophysiology* **96**, 2995–3005 (2006).

33. Mirkiani, S. *et al.* Functional motor mapping of domestic pig lumbar spinal cord using penetrating microelectrodes. *Journal of NeuroEngineering and Rehabilitation* **22**, 1–19 (2025).

34. Mushahwar, V. K., Collins, D. F. & Prochazka, A. Spinal cord microstimulation generates functional limb movements in chronically implanted cats. *Experimental neurology* **163**, 422–429 (2000).

35. Bamford, J. A., Todd, K. G. & Mushahwar, V. K. The effects of intraspinal microstimulation on spinal cord tissue in the rat. *Biomaterials* **31**, 5552–5563 (2010).

36. Ersen, A., Elkabes, S., Freedman, D. S. & Sahin, M. Chronic tissue response to untethered microelectrode implants in the rat brain and spinal cord. *Journal of neural engineering* **12**, 016019 (2015).

37. Tsui, C. T., Lal, P., Fox, K. V., Churchward, M. A. & Todd, K. G. The effects of electrical stimulation on glial cell behaviour. *BMC Biomedical Engineering* **4**, 7 (2022).

38. Polikov, V. S., Tresco, P. A. & Reichert, W. M. Response of brain tissue to chronically implanted neural electrodes. *Journal of neuroscience methods* **148**, 1–18 (2005).

39. Biran, R., Martin, D. C. & Tresco, P. A. Neuronal cell loss accompanies the brain tissue response to chronically implanted silicon microelectrode arrays. *Experimental neurology* **195**, 115–126 (2005).

40. Prasad, A. & Sanchez, J. C. Quantifying long-term microelectrode array functionality using chronic in vivo impedance testing. *Journal of neural engineering* **9**, 026028 (2012).

41. McCreery, D., Pikov, V., Lossinsky, A., Bullara, L. & Agnew, W. Arrays for chronic functional microstimulation of the lumbosacral spinal cord. *IEEE Transactions on Neural Systems and Rehabilitation Engineering* **12**, 195–207 (2004).

42. Toossi, A. *et al.* Comparative neuroanatomy of the lumbosacral spinal cord of the rat, cat, pig, monkey, and human. *Scientific Reports* **11**, 1955 (2021).

43. Toossi, A., Everaert, D. G., Azar, A., Dennison, C. R. & Mushahwar, V. K. Mechanically stable intraspinal microstimulation implants for human translation. *Annals of biomedical engineering* **45**, 681–694 (2017).

44. Lee, J. H. *et al.* A novel porcine model of traumatic thoracic spinal cord injury. *Journal of neurotrauma* **30**, 142–159 (2013).

45. Zimmermann, J. B. & Jackson, A. Closed-loop control of spinal cord stimulation to restore hand function after paralysis. *Frontiers in neuroscience* **8**, 87 (2014).

46. Toossi, A. *et al.* Effect of anesthesia on motor responses evoked by spinal neural prostheses during intraoperative procedures. *Journal of neural engineering* **16**, 036003 (2019).

47. Toossi, A. *et al.* Ultrasound-guided spinal stereotactic system for intraspinal implants. *Journal of Neurosurgery: Spine* **29**, 292–305 (2018).

48. Mirkiani, S. *et al.* Safety of mapping the motor networks in the spinal cord using penetrating microelectrodes in Yucatan minipigs. *Journal of Neurosurgery: Spine* **1**, 1–13 (2024).

49. Toossi, A., Everaert, D. G., Perlmutter, S. I. & Mushahwar, V. K. Functional organization of motor networks in the lumbosacral spinal cord of non-human primates. *Scientific Reports* **9**, 13539 (2019).

50. Borrell, J. A., Frost, S. B., Peterson, J. & Nudo, R. J. A 3D map of the hindlimb motor representation in the lumbar spinal cord in Sprague Dawley rats. *Journal of neural engineering* **14**, 016007 (2016).

51. Krüger, J., Caruana, F. & Rizzolatti, G. Seven years of recording from monkey cortex with a chronically implanted multiple microelectrode. *Frontiers in neuroengineering* **3**, 1314 (2010).

52. Wang, L. *et al.* High-density implantable neural electrodes and chips for massive neural recordings. *Brain-X* **2**, e65 (2024).

53. Obaid, A. *et al.* Massively parallel microwire arrays integrated with CMOS chips for neural recording. *Science advances* **6**, eaay2789 (2020).

54. Bamford, J. A., Lebel, R. M., Parseyan, K. & Mushahwar, V. K. The fabrication, implantation, and stability of intraspinal microwire arrays in the spinal cord of cat and rat. *IEEE transactions on neural systems and rehabilitation engineering* **25**, 287–296 (2016).

55. Cogan, S. F. Neural stimulation and recording electrodes. *Annu. Rev. Biomed. Eng.* **10**, 275–309 (2008).

56. Kelly, A. *et al.* Laser-induced periodic surface structure enhances neuroelectrode charge transfer capabilities and modulates astrocyte function. *ACS Biomaterials Science & Engineering* **6**, 1449–1461 (2020).

57. Pena, A. *et al.* Mechanical fatigue resistance of an implantable branched lead system for a distributed set of longitudinal intrafascicular electrodes. *Journal of neural engineering* **14**, 066014 (2017).

58. Memberg, W. D., Stage, T. G. & Kirsch, R. F. A fully implanted intramuscular bipolar myoelectric signal recording electrode. *Neuromodulation: Technology at the Neural Interface* **17**, 794–799 (2014).

59. Thota, A. K. *et al.* A Multi-lead Multi-electrode System for Neural-interface Enabled Advanced Prostheses. in 109–110 (IEEE, 2013).

60. Thota, A. K., Jung, R. & Kuntaegowdanahalli, S. S. Multi-lead multi-electrode management system. (2016).

61. Henderson, J. M., Schade, C., Sasaki, J., Caraway, D. L. & Oakley, J. C. Prevention of mechanical failures in implanted spinal cord stimulation systems. *Neuromodulation: Technology at the Neural Interface* **9**, 183–191 (2006).

62. Shiroff, J. A., Skubitz, J. J. & Rawat, P. B. Electrode leads for use with implantable neuromuscular electrical stimulator. (2019).

63. Machado, A. *et al.* Deep brain stimulation for Parkinson's disease: surgical technique and perioperative management. *Movement disorders: official journal of the Movement Disorder Society* **21**, S247–S258 (2006).

64. Hasoon, J. *et al.* Device-related complications associated with cylindrical lead spinal cord stimulator implants: a comprehensive review. *Current Pain and Headache Reports* **28**, 941–947 (2024).

65. Dalrymple, A. N., Jones, S. T., Fallon, J. B., Shepherd, R. K. & Weber, D. J. Overcoming failure: improving acceptance and success of implanted neural interfaces. *Bioelectronic Medicine* **11**, 6 (2025).

66. Huang, Y. *et al.* Crossed-wire laser microwelding of Pt-10 Pct Ir to 316 LVM stainless steel: part II. Effect of orientation on joining mechanism. *Metallurgical and Materials Transactions A* **43**, 1234–1243 (2012).

67. Quazi, M. M. *et al.* A comprehensive assessment of laser welding of biomedical devices and implant materials: recent research, development and applications. *Critical Reviews in Solid State and Materials Sciences* **46**, 109–151 (2021).

68. Mirkiani, S. *et al.* Overground gait kinematics and muscle activation patterns in the Yucatan mini pig. *Journal of Neural Engineering* **19**, 026009 (2022).

69. Lau, B., Guevremont, L. & Mushahwar, V. K. Strategies for generating prolonged functional standing using intramuscular stimulation or intraspinal microstimulation. *IEEE Transactions on Neural Systems and Rehabilitation Engineering* **15**, 273–285 (2007).

70. Moritz, C. T., Lucas, T. H., Perlmutter, S. I. & Fetz, E. E. Forelimb movements and muscle responses evoked by microstimulation of cervical spinal cord in sedated monkeys. *Journal of neurophysiology* **97**, 110–120 (2007).

71. Mushahwar, V. & Horch, K. Selective activation and graded recruitment of functional muscle groups through spinal cord stimulation. *Annals of the New York Academy of Sciences* **860**, 531–535 (1998).

72. Gustafsson, B. & Jankowska, E. Direct and indirect activation of nerve cells by electrical pulses applied extracellularly. *The Journal of physiology* **258**, 33–61 (1976).

73. McIntyre, C. C. & Grill, W. M. Extracellular stimulation of central neurons: influence of stimulus waveform and frequency on neuronal output. *Journal of neurophysiology* **88**, 1592–1604 (2002).

74. Formento, E. *et al.* Electrical spinal cord stimulation must preserve proprioception to enable locomotion in humans with spinal cord injury. *Nature neuroscience* **21**, 1728–1741 (2018).

75. Capogrosso, M. *et al.* A computational model for epidural electrical stimulation of spinal sensorimotor circuits. *Journal of Neuroscience* **33**, 19326–19340 (2013).

76. Hachmann, J. T. *et al.* Epidural spinal cord stimulation as an intervention for motor recovery after motor complete spinal cord injury. *Journal of neurophysiology* **126**, 1843–1859 (2021).

77. Azad, T. D. *et al.* Duraplasty in acute spinal cord injury: a systematic review. *European Spine Journal* 1–9 (2025).

78. Archavlis, E. *et al.* Pathophysiologic Mechanisms of Severe Spinal Cord Injury and Neuroplasticity Following Decompressive Laminectomy and Expansive Duraplasty: A Systematic Review. *Neurology International* **17**, 57 (2025).

79. Streijger, F. *et al.* Duraplasty in traumatic thoracic spinal cord injury: impact on spinal cord hemodynamics, tissue metabolism, histology, and behavioral recovery using a porcine model. *Journal of neurotrauma* **38**, 2937–2955 (2021).

80. Cerro, P. D. *et al.* Neuropathological and motor impairments after incomplete cervical spinal cord injury in pigs. *Journal of Neurotrauma* **38**, 2956–2977 (2021).

81. Ziu, E., Weisbrod, L. J. & Mesfin, F. B. Spinal shock. in *StatPearls [Internet]* (StatPearls Publishing, 2024).

82. Gayen, C. D. *et al.* Survival model of thoracic contusion spinal cord injury in the domestic pig. *Journal of Neurotrauma* **40**, 965–980 (2023).

83. Amiri, A. R., Fouyas, I. P., Cro, S. & Casey, A. T. Postoperative spinal epidural hematoma (SEH): incidence, risk factors, onset, and management. *The Spine Journal* **13**, 134–140 (2013).

84. Moxon, K. A. *et al.* Long-term recordings of multiple, single-neurons for clinical applications: the emerging role of the bioactive microelectrode. *Materials* **2**, 1762–1794 (2009).

85. McConnell, G. C. *et al.* Implanted neural electrodes cause chronic, local inflammation that is correlated with local neurodegeneration. *Journal of neural engineering* **6**, 056003 (2009).

86. Szarowski, D. *et al.* Brain responses to micro-machined silicon devices. *Brain research* **983**, 23–35 (2003).

87. Biran, R., Martin, D. C. & Tresco, P. A. The brain tissue response to implanted silicon microelectrode arrays is increased when the device is tethered to the skull. *Journal of biomedical materials research Part A* **82**, 169–178 (2007).

88. Nolta, N. F., Christensen, M. B., Crane, P. D., Skousen, J. L. & Tresco, P. A. BBB leakage, astrogliosis, and tissue loss correlate with silicon microelectrode array recording performance. *Biomaterials* **53**, 753–762 (2015).

89. Subbaroyan, J., Martin, D. C. & Kipke, D. R. A finite-element model of the mechanical effects of implantable microelectrodes in the cerebral cortex. *Journal of neural engineering* **2**, 103 (2005).

90. Wellman, S. M., Li, L., Yaxiaer, Y., McNamara, I. & Kozai, T. D. Revealing spatial and temporal patterns of cell death, glial proliferation, and blood-brain barrier dysfunction around implanted intracortical neural interfaces. *Frontiers in neuroscience* **13**, 493 (2019).

91. Kozai, T. D., Jaquins-Gerstl, A. S., Vazquez, A. L., Michael, A. C. & Cui, X. T. Brain tissue responses to neural implants impact signal sensitivity and intervention strategies. *ACS chemical neuroscience* **6**, 48–67 (2015).

92. Vedam-Mai, V. *et al.* The national DBS brain tissue network pilot study: need for more tissue and more standardization. *Cell and tissue banking* **12**, 219–231 (2011).

93. Orlowski, D. *et al.* Brain tissue reaction to deep brain stimulation—a longitudinal study of DBS in the goettingen minipig. *Neuromodulation: Technology at the Neural Interface* **20**, 417–423 (2017).

94. Grill, W. M. & Thomas Mortimer, J. Electrical properties of implant encapsulation tissue. *Annals of biomedical engineering* **22**, 23–33 (1994).

95. Roitbak, T. & Syková, E. Diffusion barriers evoked in the rat cortex by reactive astrogliosis. *Glia* **28**, 40–48 (1999).

96. Barrese, J. C. *et al.* Failure mode analysis of silicon-based intracortical microelectrode arrays in non-human primates. *Journal of neural engineering* **10**, 066014 (2013).

97. Suner, S., Fellows, M. R., Vargas-Irwin, C., Nakata, G. K. & Donoghue, J. P. Reliability of signals from a chronically implanted, silicon-based electrode array in non-human primate primary motor cortex. *IEEE transactions on neural systems and rehabilitation engineering* **13**, 524–541 (2005).

98. Mushahwar, V. K. & Horch, K. W. Proposed specifications for a lumbar spinal cord electrode array for control of lower extremities in paraplegia. *IEEE transactions on rehabilitation engineering* **5**, 237–243 (1997).

99. Jankowska, E. & Roberts, W. An electrophysiological demonstration of the axonal projections of single spinal interneurones in the cat. *The Journal of Physiology* **222**, 597–622 (1972).

100. Kim, Y.-T., Hitchcock, R. W., Bridge, M. J. & Tresco, P. A. Chronic response of adult rat brain tissue to implants anchored to the skull. *Biomaterials* **25**, 2229–2237 (2004).

101. Vomero, M. *et al.* On the longevity of flexible neural interfaces: Establishing biostability of polyimide-based intracortical implants. *Biomaterials* **281**, 121372 (2022).

102. Luan, L. *et al.* Ultraflexible nanoelectronic probes form reliable, glial scar–free neural integration. *Science advances* **3**, e1601966 (2017).

103. Waters, C. M. Reactive oxygen species in mechanotransduction. *American Journal of Physiology-Lung Cellular and Molecular Physiology* **287**, L484–L485 (2004).

104. Cheung, K. C. Implantable microscale neural interfaces. *Biomedical microdevices* **9**, 923–938 (2007).

105. Minev, I. R. *et al.* Electronic dura mater for long-term multimodal neural interfaces. *Science* **347**, 159–163 (2015).

106. Kathe, C. *et al.* Wireless closed-loop optogenetics across the entire dorsoventral spinal cord in mice. *Nature biotechnology* **40**, 198–208 (2022).

107. Hanson, T. L., Diaz-Botia, C. A., Kharazia, V., Maharbiz, M. M. & Sabes, P. N. The “sewing machine” for minimally invasive neural recording. *BioRxiv* 578542 (2019).

108. Bertelsen, A., Melo, J., Sánchez, E. & Borro, D. A review of surgical robots for spinal interventions. *The International Journal of Medical Robotics and Computer Assisted Surgery* **9**, 407–422 (2013).

109. Frederick, R. A., Meliane, I. Y., Joshi-Imre, A., Troyk, P. R. & Cogan, S. F. Activated iridium oxide film (AIROF) electrodes for neural tissue stimulation. *Journal of neural engineering* **17**, 056001 (2020).

110. Frederick, R. A., Troyk, P. R. & Cogan, S. F. Wireless transmission of voltage transients from a chronically implanted neural stimulation device. *Journal of Neural Engineering* **19**, 026049 (2022).

Extended Material

The developed ISMS system comprised 14 electrodes fabricated by laser micromachining (Pt-Ir 80:20%, 50 µm diameter insulated with 4µm polyimide; arranged 7 per side with ~ 6mm spacing between electrodes in the rostrocaudal direction). Electrodes were joined to microcoils using laser welding (Fig.1a, 1b). Microcoils had an outer diameter of ~190 µm made from 25µm microwires further coated with PDMS (Extended Fig. 3a). Additionally, a 14-channel coiled cable was incorporated in the system to account for the relative movement between the spinal cord and spinal column[43]. Using two Medtronic extension cables, the electrode array was connected to a custom-made, implantable wireless stimulator that could send and receive data and powered through an extracorporeal coil (Fig. 1, Extended Fig. 2). The designed array spanned at least 36 mm in the rostrocaudal dimension. Despite being smaller than the average pig lumbosacral enlargement measured based on anatomical landmarks (66.6±5.6 mm[42]), the array length proved sufficient for targeting the locomotor-related networks needed for walking in the lumbar enlargement.

Extended Figures

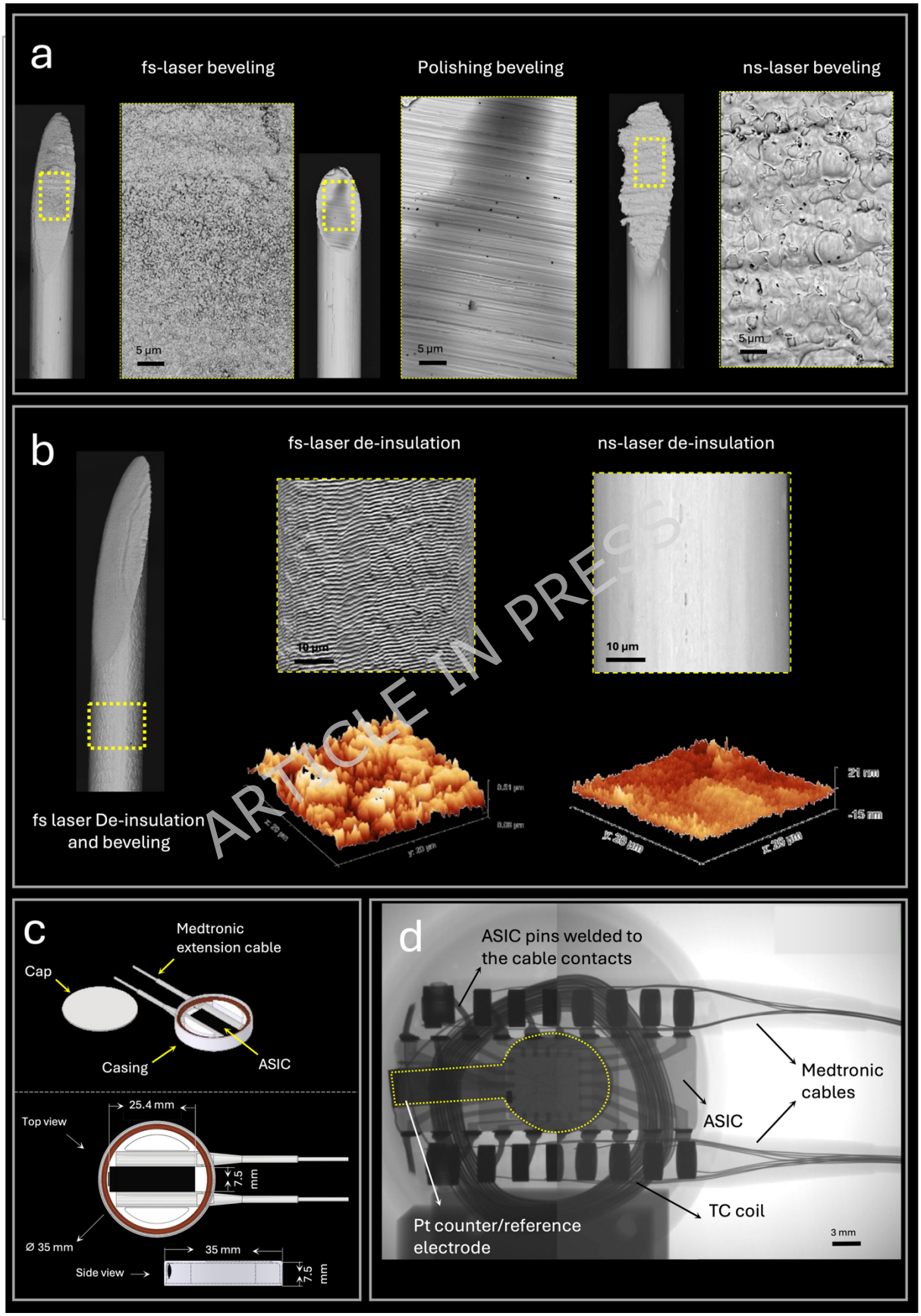

Extended Fig 1. Laser microfabrication of electrodes and the wireless stimulator. (a) *SEM images of electrodes beveled using femtosecond (fs) laser, mechanical polishing, and nanosecond (ns) laser. Polyimide insulation of microwires was removed by ns laser ablation. The insets show SEM images of the microstructure of the beveled surface at higher magnification* ***(b)*** *An electrode de-insulated and beveled using fs laser (left). SEM images of the surface microstructure of electrodes de-insulated by fs and ns lasers are shown at higher magnification. Atomic force microscopy images of the de-insulated surface shown below the SEM images demonstrate differences in surface microstructure* ***(c)*** *Schematic of the wireless stimulator, its components and dimensions.* ***(d)*** *X-ray microscopy images of the implantable wireless stimulator showing the reference/counter electrode and the Medtronic cables welded to the ASIC pins.*

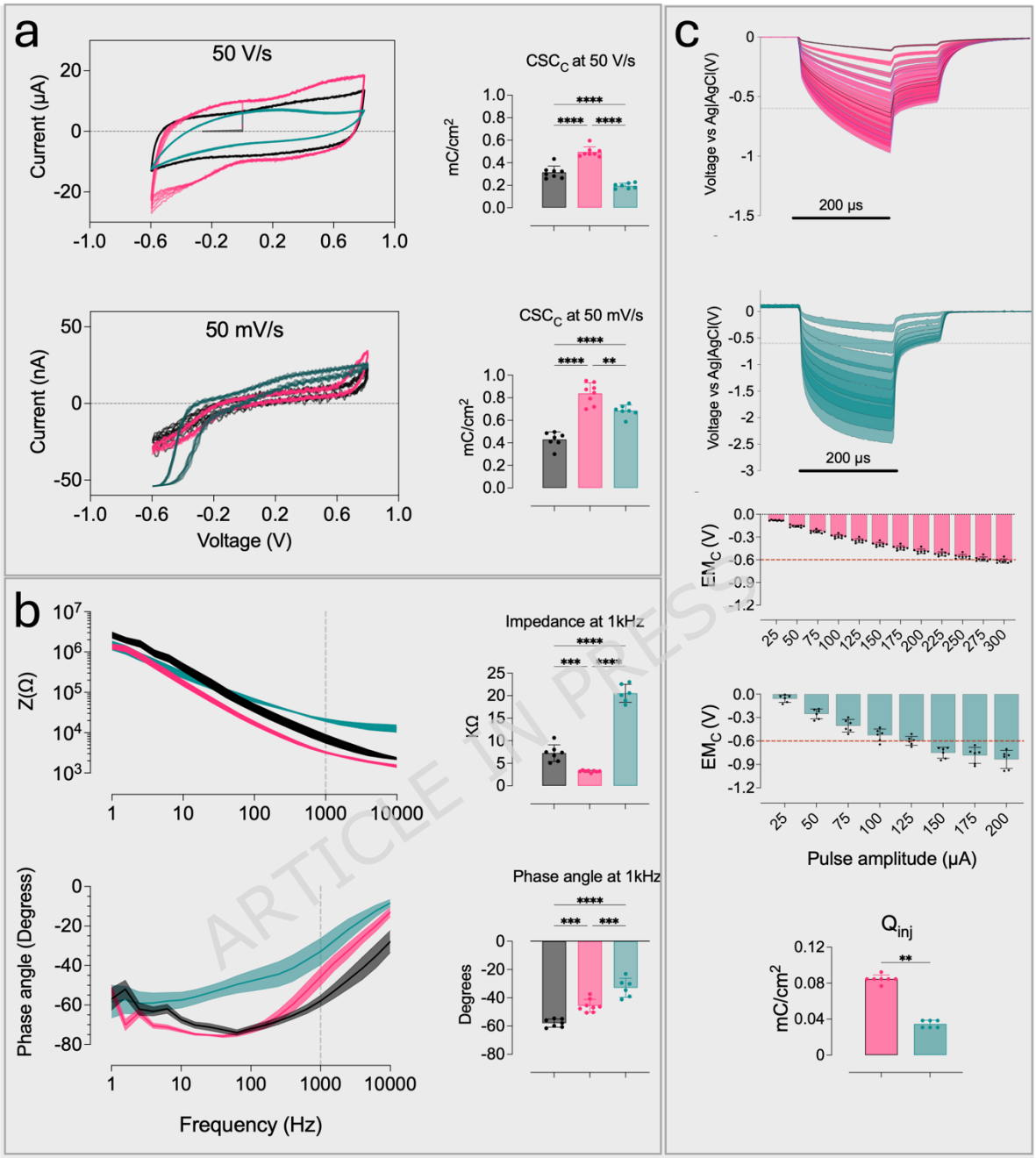
a
50 V/s
Current (µA)
20
0
-20
-1.0 -0.6 -0.2 0.2 0.6 1.0
CSC$_C$ at 50 V/s
mC/cm^2
1.0 0.8 0.6 0.4 0.2 0.0
****
****
****
50 mV/s
Current (nA)
50
0
-50
-1.0 -0.6 -0.2 0.2 0.6 1.0
Voltage (V)
CSC$_C$ at 50 mV/s
mC/cm^2
****
****
**
b
Z(Ω)
10^7 10^6 10^5 10^4 10^3
1 10 100 1000 10000
Impedance at 1kHz
KΩ
25 20 15 10 5 0
****
***
***
Phase angle (Degress)
0 -20 -40 -60 -80
1 10 100 1000 10000
Frequency (Hz)
Phase angle at 1kHz
Degrees
0 -20 -40 -60 -80
****
***
***
c
Voltage vs Ag|AgCl(V)
0 -0.5 -1
200 µs
Voltage vs Ag|AgCl(V)
0 -0.5 -1 -1.5 -2 -2.5 -3
200 µs
EM$_C$ (V)
0.0 -0.3 -0.6 -0.9 -1.2
25 50 75 100 125 150 175 200 225 250 275 300
EM$_C$ (V)
0.0 -0.3 -0.6 -0.9 -1.2
25 50 75 100 125 150 175 200
Pulse amplitude (µA)
Q$_{inj}$
mC/cm^2
0.12 0.08 0.04 0
**
in vitro - Pre-cleaning
in vitro - Post-cleaning
in vivo
d
Coiled cable
Micro-manipulator for stretching
Coiled cable immersed in PBS
Phase angle (deg)
200 100 0 -100
1E+8 1E+4 1E+0
Impedance (Ω)
1 10 100 1000 10000
Frequency (Hz)
Z (at rest)
Z (stretched)
Phase (at rest)
Phase (stretched)

Extended Fig 2. Electrochemical properties of the electrodes and coiled cable. (a) *CV diagrams at sweep rates of 50 V/s and 50 mV/s are shown for pre-cleaning, post-cleaning, and in vivo as well as calculated CSC_c for each condition.* ***(b)*** *EIS results showing the magnitude and phase angle at frequency ranges of 1-10kHz for three conditions of pre-cleaning, post-cleaning, and in vivo. The phase angle and impedance magnitude at 1kHz were calculated for each condition.* ***(c)*** *Voltage transient responses to current pulses are shown in-vitro (post-cleaning from 25 to 300 µA in 25µA steps) and in-vivo (from 25 to 200 µA in 25µA steps). The maximum cathodic potential excursion (E_{mc}) for each current amplitude and the charge injection capacity (Q_{inj}) are shown for electrodes in vitro (post-cleaning) and in vivo.* ***(d)*** *EIS measurements were used to calculate the capacitance between a single wire and the bundle of the remaining 13 wires in the coiled cable immersed in PBS at rest and stretched by 40%. EIS graphs showing the impedance and phase angle of one microwire against the remaining microwires at rest and stretched by 40%. All error bars indicate standard deviation; *p < 0.05, **p < 0.01, ***p < 0.001, ****p < 0.0001*

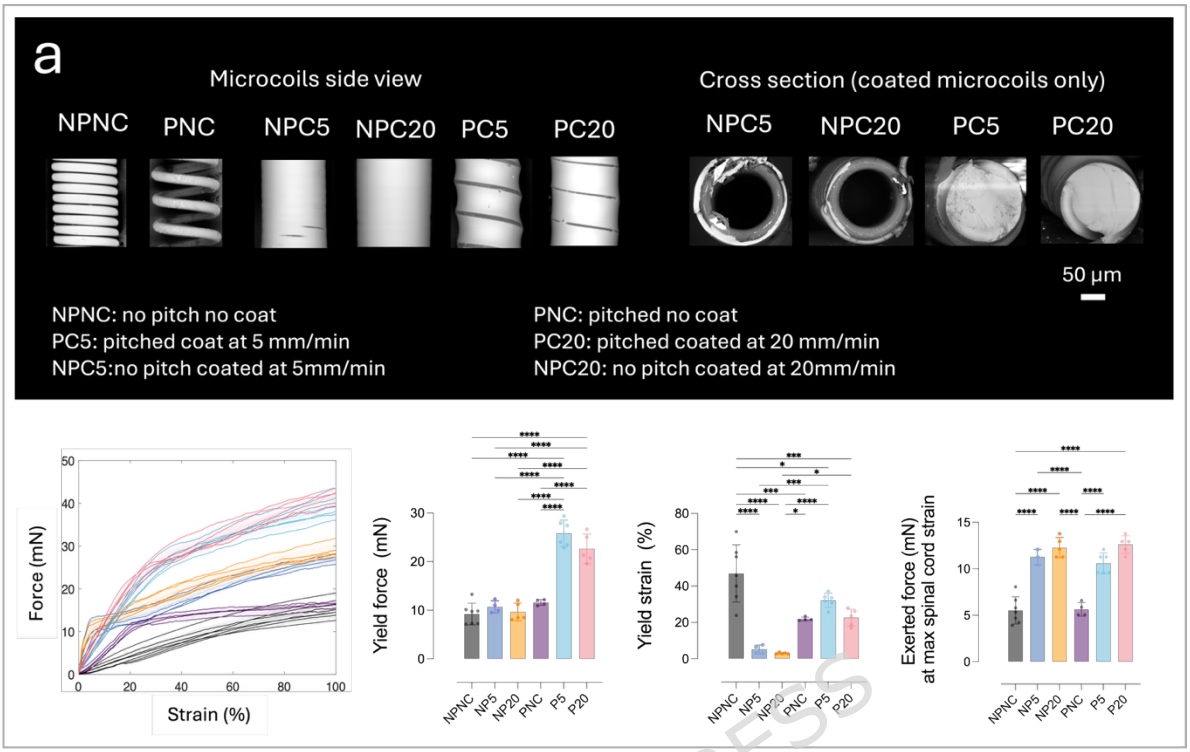

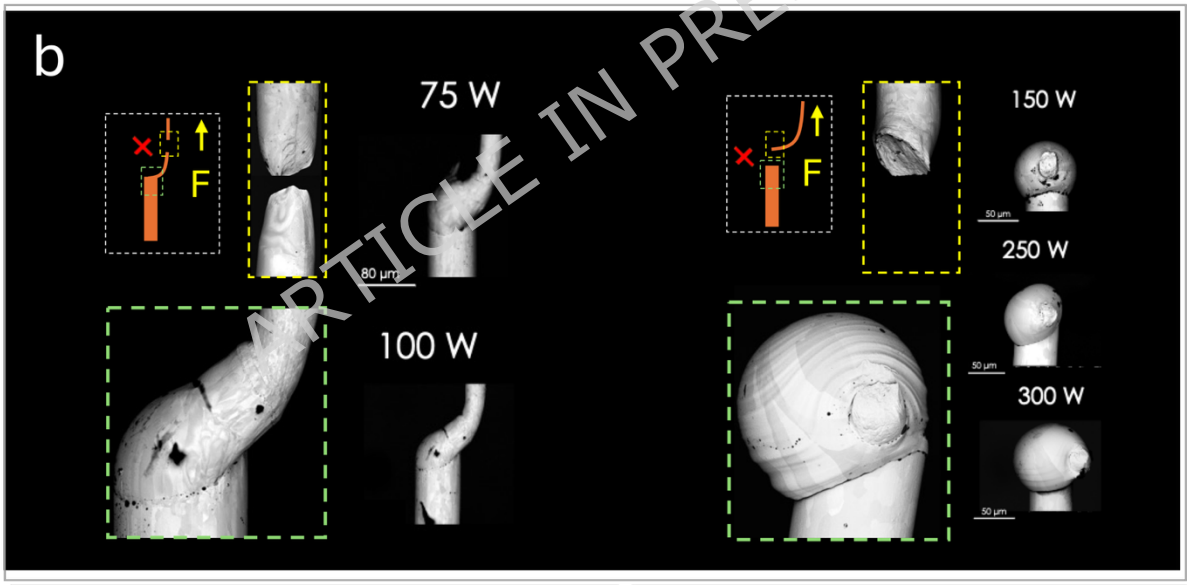

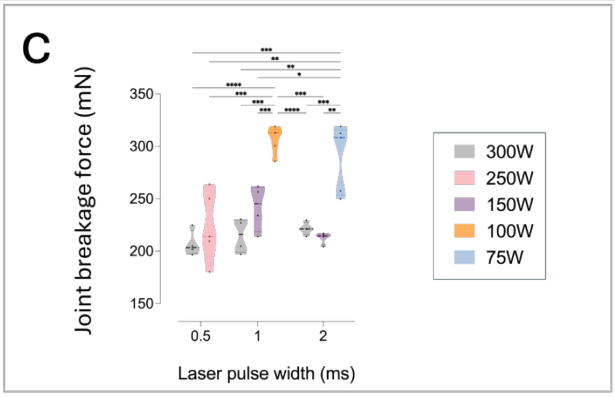

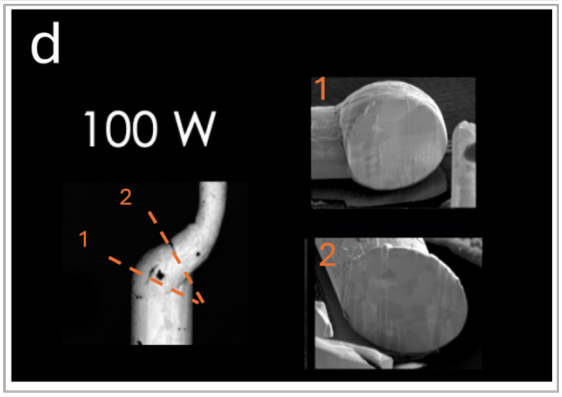

Extended Fig 3. Mechanical properties of various microcoil designs and joint breakage force (JBF) of laser welded microwires. (a) *SEM images of microcoils with and without pitch, and dip-coated into PDMS at 5 mm/min or 20 mm/min. Cross-sectional images are shown in top right indicating that the inner space of the microcoils with no pitch were not coated with PDMS. Force-strain diagrams of uniaxial tensile test on various microcoil designs are shown bottom left. Mean and standard deviation of yield force, yield strain, and force at maximum spinal cord elongation (11%) values are shown bottom right for each microcoil design.* ***(b)*** *SEM images of the weld fracture surface. Failure can occur in the smaller lead microwire (left) or at the welded junction (right).* ***(c)*** *Violin plots of JBF values at different pulse widths and laser powers.* ***(d)*** *SEM images of weld cross-section obtained by focused ion beam of a welded sample at 100W shows no impurities or porosities in the heat affected zone.*

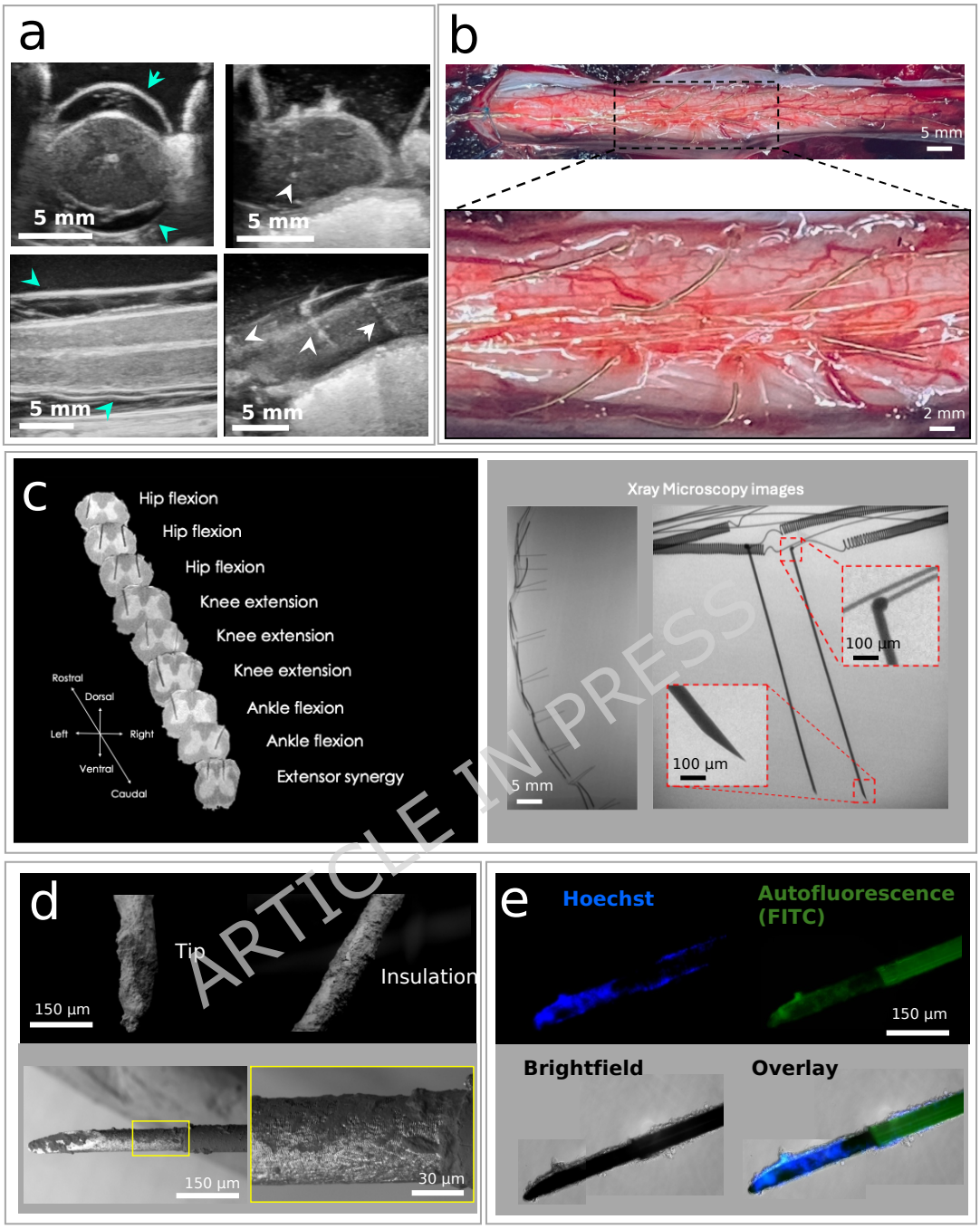

Extended Fig.4: Ultrasound guided implantation and post-mortem images of the spinal cord and explanted electrodes. (a) *Ultrasound images of spinal cord in transverse and sagittal views before opening the dura mater (left) informs the neurosurgeon of the orientation of the spinal cord and possible rotations. Blue arrows show the dura mater. The images on the right show in situ imaging of the spinal cord during implantation. Yellow arrows show the signal enhancement due to the implanted electrodes.* ***(b)*** *Optical images of the implanted array in pig spinal cord. The bottom image at higher magnification shows the microcoils and their relative size to the spinal cord.* ***(c)*** *Axial MRI images (left) and X-ray microscopy images (right) of explanted spinal cord with implanted array. MRI images on the left indicate the location of implanted electrodes, visible as regions of signal void due to magnetic susceptibility artifacts. These hypointense regions correspond to the electrode positions within the spinal cord parenchyma. X-ray images provide an overview of the electrode array's configuration along the spinal cord. Insets highlight the welded connection region and the*

electrode tip. The spinal cord tissue is not visible in the X-ray due to its low radiodensity. ***(d)*** *SEM images of the explanted electrodes after 8 days of implantation in pig spinal cord shows attachment of biological material to the electrode tip and insulation* ***(e)*** *Immunocytochemistry (ICC) images of the explanted electrodes after 14 days of implantation showed that the attached materials were cells. ICC images reveled these cells were activated microglia (not shown).*

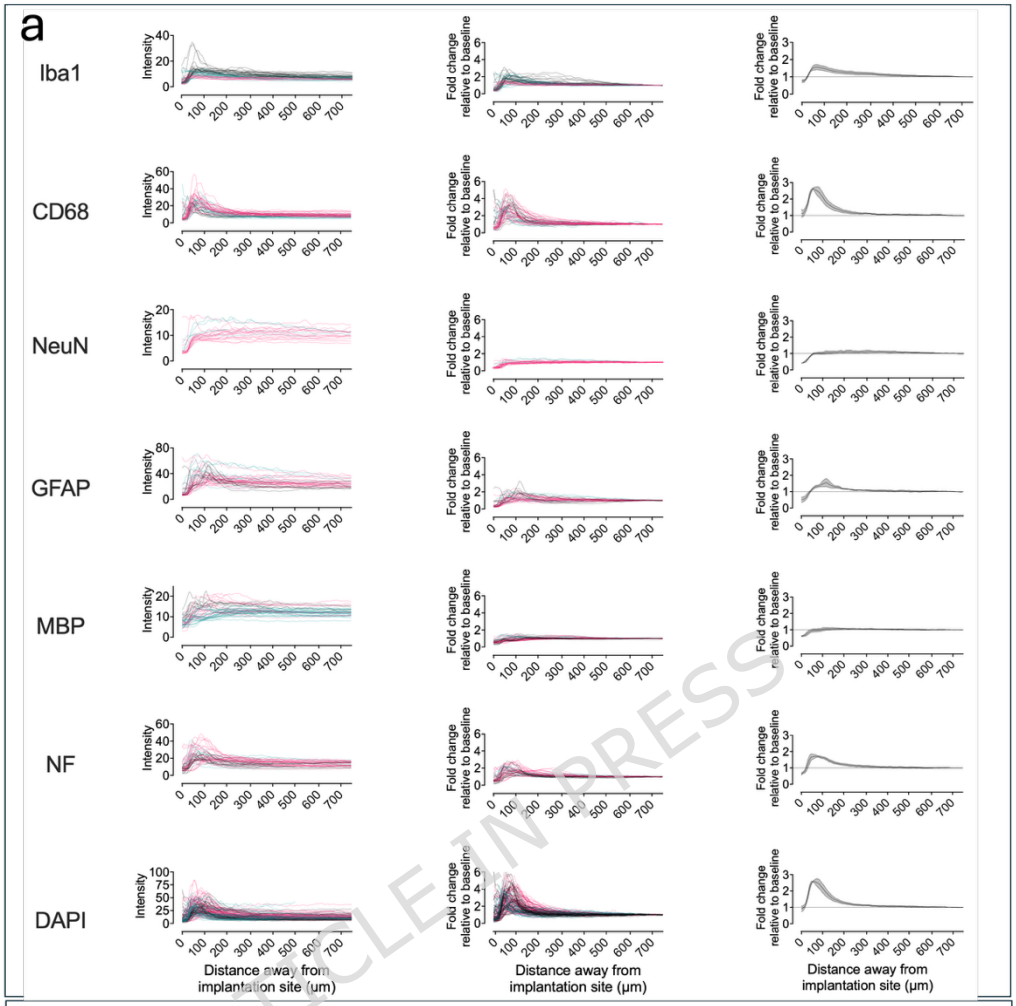

Extended Fig.5. Zonal analysis of immunoreactivity to various antibodies. (a) *Raw averaged fluorescence ring intensities, normalized to the baseline intensity 750 µm away from the center of the void caused by electrode placement, and averaged normalized values across 3 animals of immunoreactivity to Iba1, Cd68, NeuN, GFAP, MBP, NF200 and DAPI.* ***(b)*** *A representative image of coronal tissue section stained with H&E shows tissue changes around an electrode. Confocal microscopy images of immunoreactivity to GFAP, NeuN, CD68, Iba1, NF200, MBP and DAPI show high magnification images of the affected areas near* ***(c, d, e, f, g, h)*** *and further away* ***(i, j)*** *from the implanted electrode. Activated astrocytes (white) and activated microglia (pink) were confined around the electrode. Neurons (red arrow in f) at the vicinity (<50µm) of the implanted electrode were observed. Non-activated microglia (i) and astrocytes (j) are shown in a region away from the electrode on the right.*